Nonlocal microstructural mechanics of active materials

Thesis by

Kaushik Dayal

In Partial Fulfillment of the Requirements

for the Degree of

Doctor of Philosophy

California Institute of Technology

Pasadena, California

2007

(Defended 12 June, 2006.)

This thesis is dedicated to my parents

Meera and Hassan Vedanta Dayal

Acknowledgements

I am immensely grateful to Kaushik Bhattacharya for his many contributions to making my time at Caltech very enjoyable. In particular, I thank him for investing his time to encourage my learning, tolerating my methods of working and teaching me to look beyond my original problem-solving mindset for genuine insight. On a personal level, I thank him and Sohini for their friendship and the very warm interactions that we have enjoyed, his support and encouragement during various circumstances, and for always keeping my interests in mind.

I am especially grateful to Dr. G. Ravichandran and Dr. Nadia Lapusta for their advice and support regarding my future plans, their interest in my progress and for taking the time to serve on my committee.

I thank Dr. Jim Knowles for his suggestions and encouragement during our discussions in the past few years. I am especially grateful to him and Dr. Ares Rosakis for their willingness to spend their time and effort to serve on my thesis committee at very short notice. I also thank Dr. Dave Goodwin for serving on my thesis committee.

I thank Moh El-Naggar, Christian Franck, Mathias Jungen, Alex Kelly, Prashant Purohit, Yu Xiao and all the current and former members of the solids group for discussions that taught me much. I thank Kaushik Bhattacharya for initiating the weekly journal readings and the members of our group for their contributions to the discussions. I also thank Dr. Rohan Abeyaratne, Dr. Stewart Silling, and Markus Zimmerman for our discussions that were unfortunately infrequent.

I thank Sam Daly, Patrick Dondl, Moh El-Naggar, Javier, Sam Taira and all my other friends (especially those of the lunch group) for the very enjoyable time I spent in Thomas. I also thank all my friends at Caltech and elsewhere, and my former

dorm- and apartment-mates for their company.

I am very grateful to Jim Endrizzi and the International Students Program, Greg Fletcher and the Caltech Y, Sylvie Gertmenian, Maria Koeper, and Chris Silva in Thomas, and the many other staff members at Caltech who made life much more pleasant.

For financial support, I thank the Graduate Aeronautical Laboratories for the Russell R. Vought fellowship and the Division for teaching assistantships.

Above all, I thank my parents and Gautham, Lavanya and the Taras for their affection and encouragement. I thank my many cousins, aunts and uncles for their support.

Abstract

This thesis deals with two aspects of the mechanics of symmetry-breaking defects such as phase boundaries, inclusions and free surfaces, and their role in the macroscopic response of active materials. We first examine the problem of kinetics using a nonlocal theory, and then study the role of geometry in active materials with fields that are not confined to the material.

Classical PDE continuum models of active materials are not closed, and require nucleation and kinetic information or regularization as additional constitutive input. We examine this problem in the peridynamic formulation, a nonlocal continuum model that uses integral equations to account for long-range forces that are important at small scales, and allows resolution of the structure of interfaces. Our analysis shows that kinetics is inherent to the theory. Viewing nucleation as a dynamic instability at small times, we obtain interesting scaling results and insight into nucleation in regularized theories. We also exploit the computational ease of this theory to study an unusual mechanism that allows a phase boundary to bypass an inclusion.

Shifting focus to problems of an applied nature, we consider issues in the design of ferroelectric optical/electronic circuit elements. Free surfaces and electrodes on these devices generate electrical fields that must be resolved over all space, and not just within the body. These fields greatly enhance the importance of geometry in understanding the electromechanical response of these materials, and give rise to strong size and shape dependence. We describe a computational method that transforms this problem into a local setting in an accurate and efficient manner. We apply it to three examples: closure domains, a ferroelectric slab with segmented electrodes and a notch subjected to electro-mechanical loading.

Contents

List of Figures

Chapter 1

Introduction

Active materials display interesting and unusual couplings between mechanics, electromagnetics and temperature. They also often display highly nonlinear properties such as hysteresis. Active behavior is often driven by a symmetry-changing phase transformation that results in complex fine scale microstructure. The unusual properties are associated with the evolution of this microstructure under applied mechanical, electromagnetic and thermal loads. The study of active materials is an active area of research involving disciplines such as metallurgy, mechanics and applied mathematics (for example, the papers published in the journal *Smart Materials and Structures*, or proceedings of the SPIE conferences on Smart Materials: Lagoudas, 2003; Lynch, 2001; Bar-Cohen, 2001; Banks, 1993).

Current devices that exploit active materials often involve macroscopic components, in the range of hundreds of microns (for example Xu, 1991; Uchino, 1997, and references there). At such scales, continuum constitutive models that capture the average response of the material are sufficient, and it is possible to ignore the details of the various processes occurring at smaller scales (Figure 1.1).

However, future devices that are of interest will involve making smaller components that push closer to the nanometer. At these scales, microstructural details that had been averaged away to build continuum models gain importance (see Bhattacharya and James, 2005, for a perspective on these issues). It is necessary to understand microstructure more fully and build models that capture enough information to design devices at these scales, and at the same time average out atomic level pro-

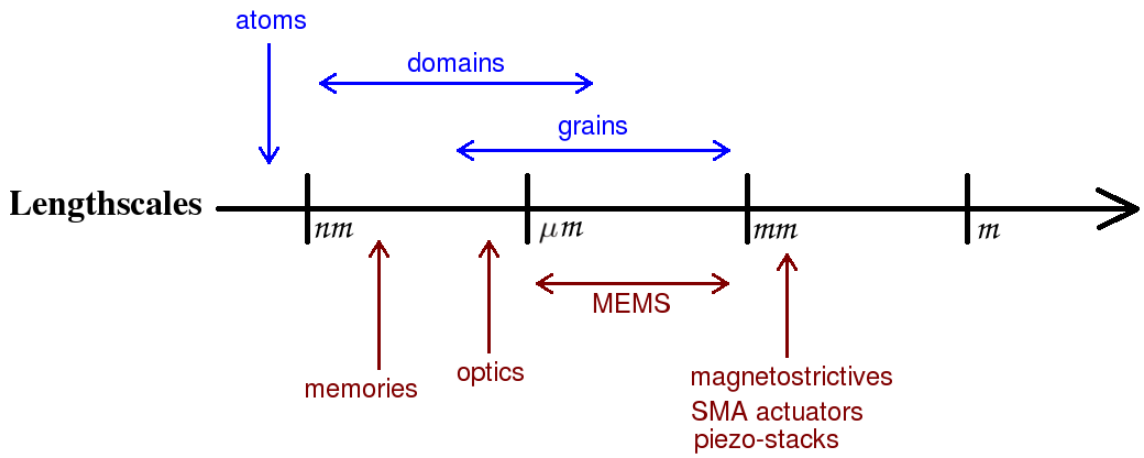

Figure 1.1: Lengthscales relevant to future device design require knowledge of the microstructural details

cesses that we are unnecessary and are significantly if not prohibitively expensive to feasibly compute.

Continuum models that capture the mechanics of microstructure are attractive due to the relative ease of solution and the availability of existing methods. In this thesis, work on two distinct problems in the general area of understanding the response of microstructure within a continuum framework is presented. We focus on crystalline materials with the active behavior driven by a first-order solid-state phase transformation that is purely displacive with no diffusion, i.e., the crystallographic unit cell changes shape discontinuously at a critical temperature.

Conventional continuum models of microstructure that examine solid-state phase transitions use non-convex strain energies to model the multiple equilibrium states of the crystallographic unit cell, using the Cauchy-Born rule to connect crystal distortions to strains. This approach has proved successful in capturing the essential physics required to understand equilibrium microstructure, and has provided insight into phenomena such as shape-memory (Bhattacharya, 2003, and references there).

However, the physics contained in this model is insufficient to understand non-equilibrium microstructural processes, i.e., the evolution of microstructure. Work by Abeyaratne and Knowles (1990) showed that the inability of the continuum strain-energy based approach to model evolution could be addressed by specifying certain

extra material information: the nucleation criterion (when interfaces form) and the kinetic relation (how fast interfaces move). Alternate approaches to this problem consisted generally of adding the missing information through regularizing strain-gradient terms. These strain-gradient methods are similar in some ways to phase-field techniques (for example in Wang et al., 1994). Both approaches raise the question of how information from processes at smaller scales can be used to extract the additional continuum constitutive laws.

The first part of this thesis examines this question using the peridynamic theory of continuum mechanics (developed independently by Kunin, 1982; Silling, 2000). The peridynamic theory is a nonlocal theory of continuum mechanics that treats continua as composed of elements that interact through long-range forces, rather than tractions. This formulation leads to integral equations rather than differential equations as the governing laws. The peridynamic model can be viewed as a heuristic continuum analog of pair-potential atomistics, or a continuum model that has some features of atomistic models, and the possibility of applying insights gained in peridynamics to atomistics exists.

The integral equations that appear in the peridynamic equations of motion involve the displacement field, but not its derivatives. This relaxes continuity and allows the peridynamic model to function as an excellent phenomenological computational tool, as defects do not require special treatment.

We present analysis and results in one dimension that suggest that nucleation in the peridynamic theory can be viewed from the perspective of stability. Numerical results suggest also that kinetics can be understood in terms of traveling waves, in the computational setting. In a two dimensional setting, we exploit the computational power of peridynamics to study an example of defect interactions.

In the second part of this thesis, we study the microstructure that forms in tetragonal ferroelectric crystals and the effect of free surfaces.

The ferroelectric materials that we study in this thesis have a spontaneous polarization below the critical Curie temperature. This spontaneous polarization can be switched between symmetry-related equilibrium states (Jona and Shirane, 1962;

Damjanovic, 1998, and references there provide much detail on the physics of ferroelectrics). As in the purely mechanical case, a non-convex energy with minima corresponding to these different equilibrium states can be used to model such a material. In the case of ferroelectrics, the energy also involves contributions from the electrostatic energy that is generated by the polarization.

Contributions to the free energy due to conventional fields, such as stress, are local and may be written as an integral over a finite region. The electrostatic energy that arises in the consideration of ferroelectrics however extends over all of space (Shu and Bhattacharya, 2001).

Conventional techniques to account for the electrostatic energy have traditionally involved periodic geometries. This allows for the use of efficient numerical techniques, and these techniques have led to insights into electromechanics of microstructure in ferroelectrics (for example, the results presented in Hu and Chen, 1998; Li et al., 2002; Wang et al., 2004). However, as device scales approach microstructural scales, there exists a need to extend these techniques to model realistic device geometries.

We present our calculations of complex geometries involving defects such as free surfaces and notches in a non-periodic setting. These calculations were performed by applying a boundary element technique to resolve the electrostatic fields, coupled to a phase-field evolution model for the polarization and strain fields.

Examples that we present include the closure domain patterns that form at a free surface, the response of a idealized device geometry to electrical forcing, and the effect of a notch on the coupling between electrical and mechanical loads.

As the two problems that this thesis deals with are quite distinct, we have reviewed the literature relevant to each problem in the corresponding chapter.

Bibliography

Abeyaratne, R., Knowles, J. K., 1990. On the driving traction on a surface of a strain discontinuity in a continuum. J. Mech. Phys. Solids 38, 345–360.

Banks, H. T. (Ed.), 1993. Mathematics in smart structures. Vol. 1919. Proceedings of the SPIE.

Bar-Cohen, Y. (Ed.), 2001. Smart Structures and Materials: Electroactive Polymers, Actuators and Devices. Proceedings of the SPIE.

Bhattacharya, K., 2003. Microstructure of martensite. Oxford University Press.

Bhattacharya, K., James, R. D., 2005. The material is the machine. Science 307 (5706), 53–54.

Damjanovic, D., 1998. Ferroelectric, dielectric and piezoelectric properties of ferroelectric thin films and ceramics. Rep. Prog. Phys. 61, 1267–1324.

Hu, H. L., Chen, L. Q., 1998. Three-dimensional computer simulation of ferroelectric domain formation. J. Am. Ceram. Soc. 81 (3), 492–500.

Jona, F., Shirane, G., 1962. Ferroelectric crystals. Oxford.

Kunin, I. A., 1982. Elastic media with microstructure. Vol. 26 of Springer Series in Solid-State Sciences. Springer-Verlag.

Lagoudas, D. C. (Ed.), 2003. Smart Structures and Materials: Active Materials: Behavior and Mechanics. Vol. 5053. Proceedings of the SPIE.

Li, Y. L., Hu, S. Y., Liu, Z. K., Chen, L. Q., 2002. Effect of substrate constraint on the stability and evolution of ferroelectric domain structures in thin films. Acta Mater. 50 (2), 395–411.

Lynch, C. S. (Ed.), 2001. Smart Structures and Materials: Active Materials: Behavior and Mechanics. Vol. 4333. Proceedings of the SPIE.

Shu, Y. C., Bhattacharya, K., 2001. Domain patterns and macroscopic behavior of ferroelectric materials. Philos. Mag. B 81 (12), 2021–2054.

Silling, S. A., 2000. Reformulation of elasticity theory for discontinuities and long-range forces. J. Mech. Phys. Solids 48, 175–209.

Uchino, K., 1997. Piezoelectric motors and ultrasonic motors. Kluwer.

Wang, J., S.-Q. Shi, L.-Q. Chen, Li, Y., T.-Y. Zhang, 2004. Phase-field simulations of ferroelectric/ferroelastic polarization switching. Acta Mater. 52 (3), 749–764.

Wang, Y. Z., Chen, L. Q., Khachaturyan, A. G., 1994. Solid-solid Phase Transformations. The Min. Metals. Mater. Soc., Ch. Computer simulation of microstructure evolution in coherent solids, pp. 245–265.

Xu, Y., 1991. Ferroelectric materials and their applications. North-Holland.

Chapter 2

Kinetics of phase transformations in the peridynamic formulation of continuum mechanics

---

Abstract

We study the kinetics of phase transformations in solids using the peridynamic formulation of continuum mechanics. The peridynamic theory is a nonlocal formulation that does not involve spatial derivatives, and is a powerful tool to study defects such as cracks and interfaces.

We apply the peridynamic formulation to the motion of phase boundaries in one dimension. We show that unlike the classical continuum theory, the peridynamic formulation does not require any extraneous constitutive laws such as the kinetic relation (the relation between the velocity of the interface and the thermodynamic driving force acting across it) or the nucleation criterion (the criterion that determines whether a new phase arises from a single phase). Instead, this information is obtained from inside the theory simply by specifying the inter-particle interaction. We derive a nucleation criterion by examining nucleation as a dynamic instability. We find the induced kinetic relation by analyzing the solutions of impact and release problems, and also directly by viewing phase boundaries as traveling waves.

We also study the interaction of a phase boundary with an elastic non-transforming inclusion in two dimensions. We find that phase boundaries remain essentially planar

with little bowing. Further, we find a new mechanism whereby acoustic waves ahead of the phase boundary nucleate new phase boundaries at the edges of the inclusion while the original phase boundary slows down or stops. Transformation proceeds as the freshly nucleated phase boundaries propagate, leaving behind some untransformed martensite around the inclusion.

2.1 Introduction

The shape-memory effect consists of the recovery of apparently plastic deformations of a specimen below a critical temperature, by heating the specimen above this critical temperature. A diffusionless solid-state or martensitic phase transformation is responsible for this effect. The apparently plastic deformation does not come about by lattice slip, but is instead caused by the motion of twin or phase boundaries. It is the kinetics of this motion that is studied here.

In classical continuum theory, these phase transforming materials have been modeled using an energy that has multiple minima, each minimum corresponding to a particular phase or variant of martensite. In a dynamic, or even quasistatic, setting, the usual constitutive information, strain energy density as a function of strain, is insufficient to determine a unique solution. For example, even simple Riemann problems with a single phase or twin boundary in the initial conditions allow a one-parameter family of solutions. Therefore, we require further material information to pick the physically correct solution. Abeyaratne and Knowles (1990, 1991b) have proposed that this extra information may be specified in the form of a nucleation criterion and a kinetic relation.

The nucleation criterion determines whether a new phase will nucleate from a single phase. The kinetic relation determines the kinetics or the rules that govern the evolution of the phase boundary. It relates the velocity to a thermodynamic driving force, these being conjugate variables in the dissipation (or entropy) inequality. The driving force is related to Eshelby's idea of the force acting on a defect (Eshelby, 1956, 1975). The nucleation criterion and the kinetic relation provide uniqueness and

well-posedness to initial-boundary value problems. Physically, they can be thought of as a macroscopic remnant of the lattice level atomic motion from one energy well to another that is lost in the continuum theory. However, a systematic derivation from a microscopic theory as well as experimental confirmation remain a topic of active research.

Another approach to overcome the inability of classical continuum mechanics to model the kinetics of phase transformations is to regularize or augment the theory, notably by adding a strain gradient (capillarity) and viscosity to the constitutive relation. This augmented theory leads to a unique solution for the motion of phase boundaries (Abeyaratne and Knowles, 1991a; Truskinovsky, 1993). Further, Abeyaratne and Knowles (1991a) have shown a correspondence between such methods and the kinetic relation. However, nucleation is incompletely explored in this theory, and computational evidence suggests that it is, in fact, quite difficult. Further, this theory leads to fourth-order equations that are difficult to deal with computationally: they are stiff and one needs smooth elements in the finite element method (see, for example, Kloucek and Luskin, 1994; Dondl and Zimmer, 2004).

There is a closely-related phase-field approach (see, for example, Artemev et al., 2001; Wang et al., 1994) in the infinitesimal strain setting. Here, one uses the transformation strain as an internal variable or order parameter, considers the free energy density as a function of this order parameter and uses linear elasticity to penalize the incompatibility in this internal variable field. This leads to a second order equation that is computationally attractive. However, the equilibrium and the dynamics can be different from that of the regularized theories described earlier (Bhattacharya, 2003). The connection between this theory and kinetic relations remains unexplored (Killough, 1998, has some discussion on this question), nucleation remains difficult and most studies are quasistatic.

The peridynamic formulation is a nonlocal continuum theory that does not use the spatial derivatives of the displacement field (Silling, 2000; Silling et al., 2003; Kunin, 1982). Briefly, any two infinitesimal volume elements interact in this theory through a spring whose force depends on their position in the reference configuration and

relative displacement. The same equations of motion are applicable over the entire body and no special treatment is required near or at defects. These properties make it a powerful tool to model problems that involve cracks (Silling and Kahan, 2004), interfaces, and other defects. This paper studies the kinetics of phase boundaries in the peridynamic formulation of continuum mechanics.

We introduce the peridynamic equation in one dimension in Section 2.2. We provide a constitutive relation that is the analog of the widely-used trilinear material. We also propose a means of introducing viscosity into the peridynamic equations without introducing spatial gradients. We conduct quasistatic and dynamic numerical experiments in Sections 2.3 and 2.4 respectively. The absence of any spatial derivatives makes this relatively easy. Importantly, we find that phase boundaries nucleate and propagate naturally and uniquely in this theory with no need for any additional constitutive information like a kinetic relation or a nucleation criterion.

We examine nucleation in Section 2.5 by viewing it as a dynamic instability. This is different from the classical treatment of nucleation (Olson and Roitburd, 1992; Ball and James, 2005; Christian, 1975). In that treatment, one introduces perturbations with strains in the other well or phase (i.e., beyond the energy peak) and examines whether this perturbation lowers the total energy of the system. Our approach also differs from that of Abeyaratne and Knowles (1990), where the criterion for nucleation is based on the thermodynamic driving force.

In contrast, we examine conditions under which a single phase solution becomes dynamically unstable. Therefore, it is not necessary to have perturbations that reach into the other well (i.e., other stable phase). Instead, one can have nucleation when the strains reach the stability (convexity) limit of one phase. We are unaware of any other studies of nucleation from this viewpoint.

Our analysis introduces a notion of a defect size that has dimensions of length and is a measure of how many springs are in a stable state and how many are not. It depends on the physical region that is unstable, but also on how close the ambient strain is to the critical strain. We propose, based on stability considerations, that nucleation occurs when this defect size reaches a critical value, and show that this is

consistent with our numerical simulations.

The kinetics of phase boundaries is examined in Section 2.6 by viewing the phase boundaries as traveling waves motivated by our numerical studies and following Abeyaratne and Knowles (1991a), Purohit (2001) and Truskinovsky and Vainchtein (2005). We show that we can use these to derive a (viscosity-dependent) kinetic relation, and that this is consistent with the results of our numerical simulations.

We turn to two dimensions in Section 2.7. We propose a two-well constitutive relation that is appropriate for two variants generated by a square-to-rectangle transformation. We study the problem of a phase boundary driven towards a non-transforming elastic precipitate. Real materials often contain such defects. Indeed, in NiTi which is the most widely use shape-memory alloy, nickel- or titanium-rich precipitates are introduced to increase the plastic yield strength. We find that the phase boundary does not deviate from its planar configuration of preferred normal even when encountering the large residual strain field of the precipitate. Further, in an intermediate range of driving force, we find that the phase transformation proceeds by nucleating a new phase boundary ahead of the inclusion while the original phase boundary stops behind it resulting in long slivers of untransformed material around the inclusions.

We conclude in Section 2.8 with a short discussion of our results.

2.2 Formulation in one dimension

The peridynamic equation of motion at a point in a homogeneous body is postulated to be (Silling, 2000)

$$\rho\partial_{tt}\mathbf{u}(\mathbf{x},t) = \int_{\mathcal{R}} \mathbf{f}(\mathbf{u}(\mathbf{x}',t)-\mathbf{u}(\mathbf{x},t),\mathbf{x}'-\mathbf{x})dV_{\mathbf{x}'} + \mathbf{b}(\mathbf{x},t) \tag{2.1}$$

where $\mathbf{x}$ is the reference configuration coordinates, $\mathbf{u}(\mathbf{x})$ is the displacement field, $\mathbf{f}(\delta\mathbf{u},\delta\mathbf{x})$ is the force between two volume elements with separation in the reference $\delta\mathbf{x} := \mathbf{x}'-\mathbf{x}$ and relative displacement $\delta\mathbf{u} := \mathbf{u}(\mathbf{x}',t)-\mathbf{u}(\mathbf{x},t)$, $\mathbf{b}(\mathbf{x},t)$ is the body

force per unit volume in the reference and ρ is the density in the reference. We also refer to $\mathbf{f}(\delta\mathbf{u}, \delta\mathbf{x})$ as the spring force. This spring force is the constitutive input in the peridynamic formulation. See Silling (2000) for a discussion of the general properties of this formulation.

We specialize to a one-dimensional setting of a slab of infinite lateral extent and of length L undergoing uniaxial longitudinal deformations. The peridynamic equation of motion may now be written as

$$\rho\partial_{tt}u(x,t) = \int_0^L f(u(x',t) - u(x,t), x' - x)dx' + b(x,t). \tag{2.2}$$

We have to specify the spring force f. We assume that this spring force is of the form

$$f(\delta u, \delta x) = F\left(\frac{\delta u}{\delta x}\right) h(\delta x) \tag{2.3}$$

with h decaying rapidly. It is easily shown that this form ensures the right scaling for the energy in the large body limit. We may view $\delta u/\delta x$ as a pairwise strain measure, F as the strain dependent force and h as the range-dependent strength of the interaction.

We model phase transforming materials by assuming that F has a trilinear form with two stable branches of equal modulus and one unstable branch with modulus equal in magnitude but negative. We assume that h decays with a length-scale l_0. Thus:

$$f(\delta u, \delta x) = E\frac{\delta x}{l_0^3}\, e^{-(\delta x/l_0)^2} \times \begin{cases} \frac{4}{\sqrt{\pi}}\left(\frac{\delta u}{\delta x} + \epsilon_0\right) & \text{if } \frac{\delta u}{\delta x} \leq -\frac{\epsilon_0}{2} \\ \frac{4}{\sqrt{\pi}}\left(-\frac{\delta u}{\delta x}\right) & \text{if } -\frac{\epsilon_0}{2} < \frac{\delta u}{\delta x} < \frac{\epsilon_0}{2} \\ \frac{4}{\sqrt{\pi}}\left(\frac{\delta u}{\delta x} - \epsilon_0\right) & \text{if } \frac{\delta u}{\delta x} \geq \frac{\epsilon_0}{2} \end{cases} \tag{2.4}$$

An advantage of this trilinear form is that it allows one to focus on phase boundaries which remain as the only nonlinearities. Note that $F(\delta u/\delta x)$ is dimensionless.

To gain some insight into this relation, consider homogeneous deformations. It is possible to define a stress for such deformations (Silling, 2000). In one dimension, it

is

$$\sigma(x) = \int_0^x \int_x^L f(u(x') - u(\hat{x}), x' - \hat{x})\, dx'\, d\hat{x}\,. \tag{2.5}$$

We note for future use that in light of the decay, this formula may also be used whenever the deformation is homogeneous on a length-scale larger than l_0. The macroscopic stress-strain curve for the microscopic force law in (2.4), calculated by assuming a homogeneous deformation, is shown in Figure 2.1. We also define an elastic modulus for this material[1] using the expression $\frac{d\sigma}{d\epsilon}$ and, not surprisingly, it is equal to the constant E in the stable low and high strain phases and $-E$ in the unstable phase.

While solving the initial-boundary value problem associated with the peridynamic equation of motion, we found that it would be useful to have a dissipative mechanism. The usual method of adding viscosity involves terms containing the strain rate (Abeyaratne and Knowles, 1991a), but this goes against the goal of peridynamics of eliminating spatial derivatives from the formulation. Hence, we add viscosity directly to the interaction force by transforming it in the manner $f \mapsto f + \nu \frac{l_0}{\delta x} \partial_t (\delta u/c) h(\delta x)$, where ν is the dimensionless coefficient of viscous damping, and $c = \sqrt{E/\rho}$ is the acoustic velocity in the long wavelength limit (see Weckner and Abeyaratne (2005) for a discussion of dispersion in peridynamic materials). Lei et al. (2006) have used a similar formulation of damping in a different context.

We now non-dimensionalize the evolution equation and assign numerical values to the parameters that define the material. Multiplying (2.2) by $\frac{l_0}{E}$, we obtain

$$\begin{aligned} \frac{l_0}{c^2} \partial_{tt} u(x,t) = & \quad \frac{l_0}{E} b(x,t) + \frac{l_0^2}{E} \int_0^{\frac{L}{l_0}} F\left(\frac{u(x',t) - u(x,t)}{x' - x}\right) h(x' - x) d\left(\frac{x'}{l_0}\right) \\ & + \quad \frac{\nu}{c} \frac{l_0^3}{E} \int_0^{\frac{L}{l_0}} \partial_t \left(u(x',t) - u(x,t)\right) \frac{h(x' - x)}{x' - x} d\left(\frac{x'}{l_0}\right). \end{aligned} \tag{2.6}$$

We set $\rho = 1$, $l_0 = 1$, $\epsilon_0 = 0.1$ and $E = \frac{\sqrt{\pi}}{4}$ for the the remainder of the paper. We usually set the length of the slab $L = 200$, but for faster phase boundaries, we use longer slabs to allow the acoustic wave and phase boundary to be sufficiently distant

[1] This definition makes it equivalent to the classical elastic modulus in uniaxial deformation.

for our analysis. Our results (nucleation and kinetics) are independent of L as long as $L \gg l_0$.

In the next couple of sections, we conduct numerical experiments with this material. We use a spatial discretization where we replace the integral over the body with a sum,

$$\int_0^L f(u(x',t) - u(x_j,t), x' - x_j)dx' \approx \sum_{i=1}^{N} f(u_i(t) - u_j(t), x_i - x_j)\Delta x, \tag{2.7}$$

and march forward in time with an explicit linear acceleration scheme. We use $\Delta x = 0.1$ for the spatial discretization, and the relation $\frac{\Delta x}{\Delta t} = 20\sqrt{\frac{E}{\rho}}$ for the time step so that we satisfy the CFL criterion for a classical wave equation with a large margin. We believe that since $l_0 \gg \Delta x$, this value of grid spacing is sufficient to approximate the integrals to be evaluated, and numerical tests show sufficient convergence of the results. A detailed numerical analysis would be interesting, but beyond the scope of this paper.

2.3 Quasistatics in one dimension

We begin our numerical exploration of the peridynamic trilinear material by studying the quasistatic response for both hard and soft loading. To obtain a quasistatic response, we start with an equilibrium state, increment the load or end displacement as appropriate, and solve (2.6) with a very large viscosity ν till such time that it reaches equilibrium, and iterate. Peridynamics requires some care for the application of the end conditions and their increment, and these are discussed below. The results are shown in Figure 2.1 superposed over the stress response for uniform strain fields.

2.3.1 Hard loading

We start these calculations with an equilibrium state with average strain deep in the low strain phase. We apply successive increments of displacement using the boundary layers (rather than boundary points due to the nonlocal nature of peridynamics).

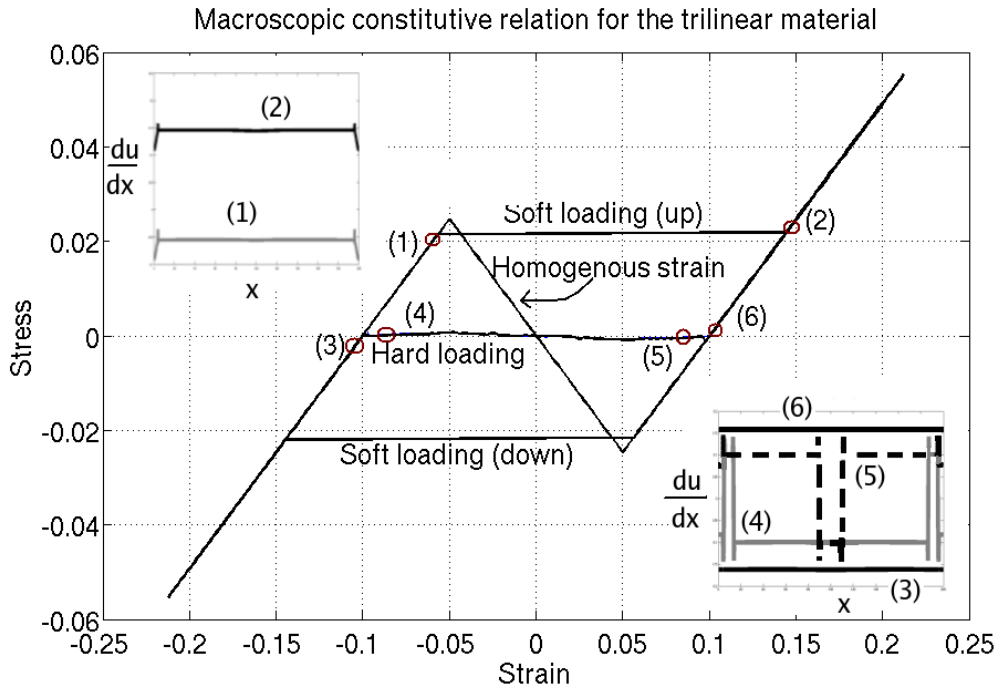

Figure 2.1: The strain-stress curve for hard and soft loading, superposed over the homogeneous strain response.

Starting with the entire bar in the low strain phase as described above, the relative displacement of the clamped ends is increased (equally but in opposite sense in the two ends to keep the calculation symmetric) to provide a given net strain increment to the bar. The strain in the clamped regions is also raised to correspond to this new average strain. The bar is then equilibrated by evolving the displacement field using the peridynamic equation of motion (2.6) with a large value of viscosity. The stress is calculated by using the formula (2.5) at some point in the interior where the deformation is homogeneous. This procedure is repeated by raising the strain until the entire bar is completely in the high strain phase. The strain is subsequently reduced in a similar manner till the bar returned to its original low strain state. The results are shown in Figure 2.1 along with the strain ($\frac{du}{dx}$) profiles at selected points.

We see that the material leaves the low-strain curve close to the so-called Maxwell stress, suffers strain increments at constant stress till it reaches the high-strain curve and then follows it. It behaves analogously as the strain is lowered. Recall that the Maxwell stress is defined as the stress at which the net signed area between

a horizontal line and the stress-strain curve is zero and corresponds to the value of stress at which the exchange of absolute stability occurs between the low and high strain phase. The strain field corresponding to the point (3), before nucleation, shows uniform strain in the bar. The strain field corresponding to point (4), soon after nucleation, shows that phase boundaries nucleate at the ends of the bar. There are two pairs of phase boundaries, one at each end. The strain away from the phase boundary is close to the equilibrium values of the two phases. The outer phase boundary at each end remains fixed in position at the grips while the inner one migrates as the applied displacement increases. The strain field corresponding to point (5), shows the inner phase boundaries about to meet each other. The strain field point (6) shows that the bar is entirely in the high strain phase. A similar process takes place on the downward path.

Note from the insets that the strain fields show an overshoot and an undershoot around the phase boundary as it transitions between the two states. This is a common feature of models of phase transitions; for example, see Purohit (2001) and Zimmermann (2002). We shall study the detailed structure of the phase boundaries in subsequent sections.

2.3.2 Soft loading

Soft loading calculations are performed by applying a uniform body force in the boundary layers as described in Silling (2000). We start with a body force that causes sufficient compression for the entire bar to be in the low strain phase. The body force is increased incrementally, the bar is equilibrated after each increment by solving (2.6) with large dissipation, and the procedure repeated till the entire bar is in the high strain phase. Subsequently the stress is incrementally decreased in a similar manner till the bar returns to its initial low strain state. The resulting stress-strain curve as well as the strain field in the bar at the points marked (1) and (2) on the stress-strain curve are shown in Figure 2.1.

The average strain is seen to follow the low strain phase until almost the peak

stress. Phase boundaries nucleate at the ends of the bar, at the strain singularities, and move at high velocity to meet at the center and transform the entire bar into the high strain state. This nucleation and meeting of the phase boundaries occurs within one load step (1% of the peak-to-valley stress difference). The material then follows the stress response curve of the high strain phase. A similar sequence occurs on the downward path.

We discuss the differences in the hard and soft loading response in Section 2.5 after we have looked at dynamic situations.

2.4 Dynamic phase boundaries in one dimension

We now study the initial-boundary value problem associated with (2.2) and solve by marching forward in time. We consider two classes of problems, release (Riemann) and impact. These classes of problems play an important role in the classical theory; having solutions to them assures existence of solutions to all initial-boundary value problems (Lefloch, 1993).

2.4.1 Release problems

In the release or Riemann problem, we seek to study the evolution of the displacement from a piecewise affine initial condition. To set up the initial condition, we obtain an equilibrium strain field with a phase boundary and then transform it using $\epsilon(x) \mapsto A\epsilon(x) + B$ so that we obtain a piecewise constant but unequilibrated strain field with a non-zero driving force across the phase boundary. The boundary conditions are applied through clamped regions with the strain held uniform and constant at the initial value.

The calculations are performed for various initial driving forces across the interface. Sequences of snapshots of the displacement fields for low, moderate and high driving forces are shown in Figure 2.2 for both viscous ($\nu = 0.333$) and inviscid materials. The overall structure of the solution is shown in Figure 2.3(a). The movement

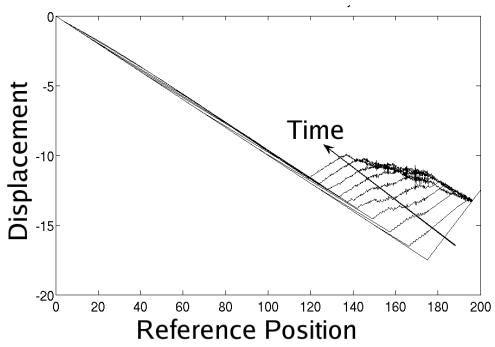

(a) Low driving force, inviscid

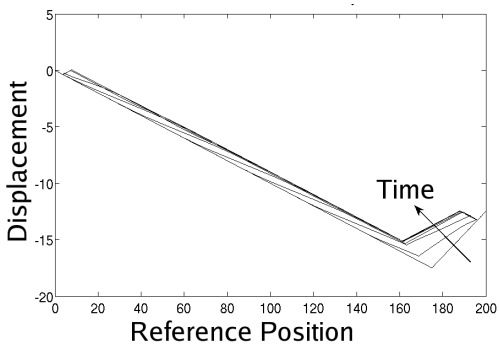

(b) Low driving force, viscous

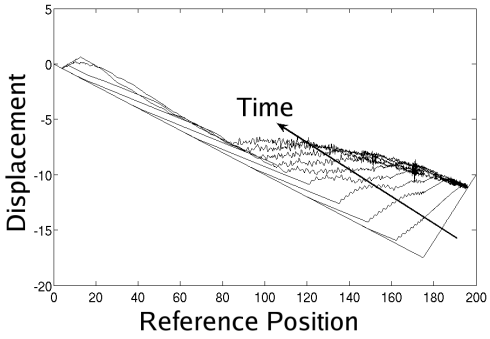

(c) Moderate driving force, inviscid

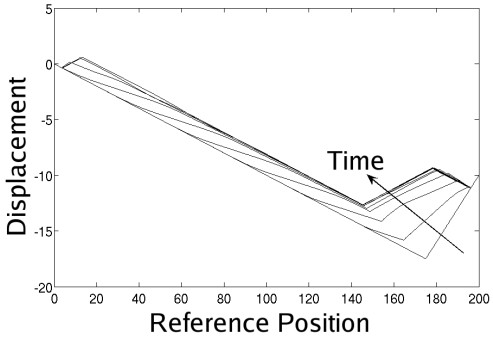

(d) Moderate driving force, viscous

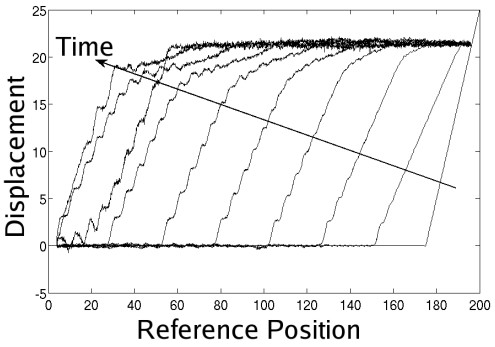

(e) High driving force, inviscid

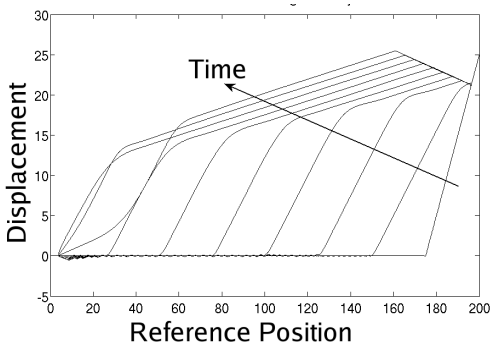

(f) High driving force, viscous

Figure 2.2: Snapshots of the displacement field in the release problem.

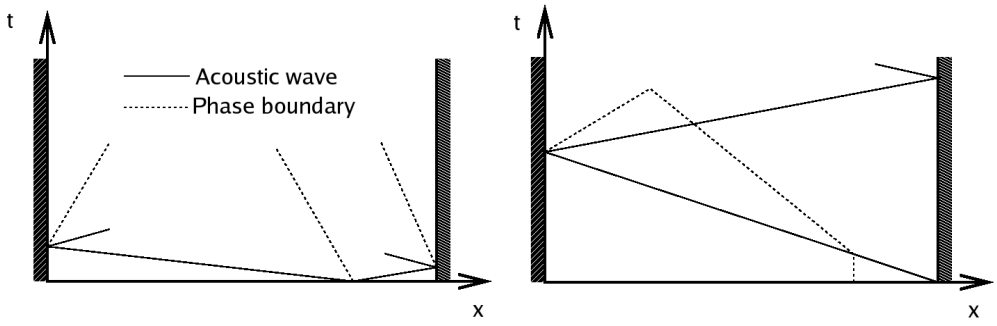

(a) Release problem (b) Impact problem

Figure 2.3: Schematic $x - t$ plane diagram for the release and impact problems

of the phase boundary can be easily followed from the displacement field by noting that the high strain phase has positive strain and thus positive slope, and the low strain phase has negative strain and thus negative slope. A change in slope without change in sign of the slope indicates an acoustic wave. All the calculations shown involve the original phase boundary moving to the left and the displacement increasing with time.

Since the initial phase boundary is not at equilibrium, it begins moving in the direction of the driving force, sending out acoustic waves in both directions. The phase boundary evolves to a steady profile quite rapidly. The acoustic waves that are sent out by the phase boundary hit the clamped ends of the bar, and reflect back into the domain. They may also nucleate phase boundaries at the ends of the bar. These phase boundaries then move back into the interior of the bar. Depending on the average strain in the bar (imposed through the initial conditions by the clamping positions of the ends of the bar), the phase boundaries can merge and form an entirely low or high strain bar, or equilibrate to some mixture of high and low strain phases.

One feature of the solution that can be seen in Figure 2.2 is that viscosity plays an important role in removing the short wavelength oscillations behind the phase boundary. As is expected in the peridynamic theory, these short waves have very small velocity (Silling, 2000). Using dissipation to remove them helps clarify the displacement field without changing the kinetics significantly. Viscosity also seems

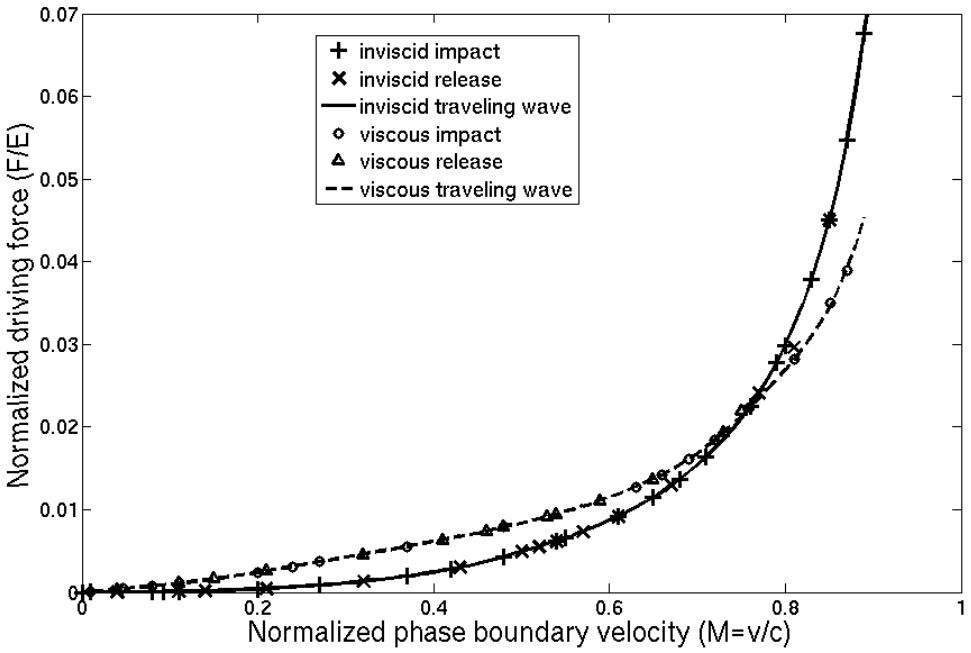

Figure 2.4: The kinetic relation induced by peridynamics. The points are results extracted from the dynamic simulations, whereas the curves are the results of traveling wave calculations.

to encourage nucleation at the clamped boundaries of the bar, as can be seen by comparing Figures 2.2(a) and 2.2(b).

We also observe from our solutions that the phase boundaries travel at constant velocity (after an initial startup stage) and maintain their shape. We examine whether the motion of these interfaces follow a kinetic relation as postulated by Abeyaratne and Knowles (1991b). To this end, we calculate the driving force across the phase boundary defined as (Abeyaratne and Knowles, 1991b):

$$F = [\![W(\epsilon)]\!] - \frac{1}{2}\left(\sigma(\epsilon_+) + \sigma(\epsilon_-)\right)[\![\epsilon]\!] \tag{2.8}$$

where $[\![g]\!] := g_+ - g_-$ is the jump across the phase boundary of the quantity g, W is the stored elastic energy, σ is the stress, and ϵ is the strain. Since the phase boundary in the peridynamic formulation is not a sharp interface separating two regions of uniform deformation as in the conventional continuum theory, we use the average

of the strain fields on either side of the phase boundary (ensuring that there are no other waves within the averaging window). We plot driving force F (normalized by E) versus velocity v (normalized by c, $\mathsf{M} = v/c$) in Figure 2.4. The results of various release calculations appear to collapse onto a single curve. This suggests that the peridynamic theory does in fact induce a kinetic relation. We shall return to study this curve in Section 2.6.

2.4.2 Impact problem with initial phase boundary

We now turn to impact problems where an equilibrium strain field with a phase boundary in the interior is used as initial condition. One end of the bar is clamped, and the other end is pulled at a constant velocity for all $t > 0$. The clamped end has uniform and constant strain equal to the equilibrium strain at $t = 0$, and this region is not evolved in time. The pulled end is subjected to a constant and uniform velocity, so that its strain remains constant and uniformly equal to the other equilibrium strain at $t = 0$.

Snapshots of the displacement fields for low, moderate and high impact velocities are shown in Figure 2.5 for both viscous ($\nu = 0.333$) and inviscid materials. The overall features of the solution are shown in Figure 2.3(b). The phase boundaries and acoustic waves can be identified and followed as described in the release problem. The ordering of the displacement fields in time can be seen by looking at the right end of the bar, that is being pulled at a constant positive velocity. The greater the displacement at the right end, the further in time the snapshot.

The initial impact sends an acoustic wave into the bar, which reaches the phase boundary and sets it into motion. The acoustic wave then goes ahead of the phase boundary and reaches the clamped end, where it reflects back into the bar, possibly nucleating another phase boundary there. The second phase boundary, when it exists, moves behind the acoustic wave and meets the original phase boundary and they annihilate each other leaving the entire bar in a high strain state. If the second phase boundary does not nucleate, the original phase boundary reaches the end of the bar,

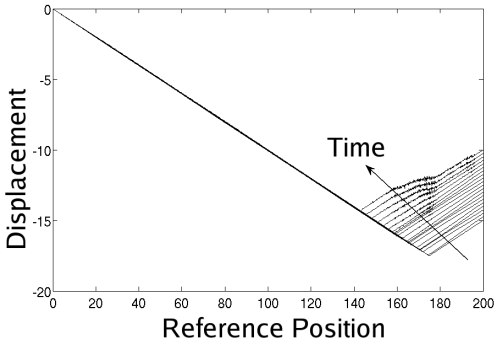

(a) Low velocity, inviscid

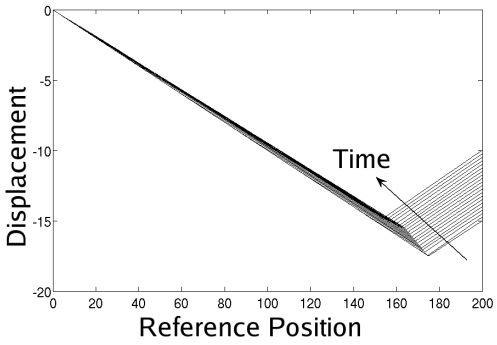

(b) Low velocity, viscous

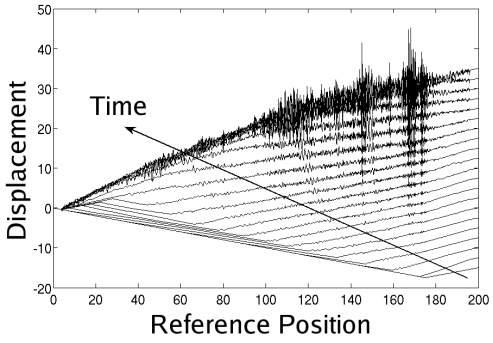

(c) Moderate velocity, inviscid

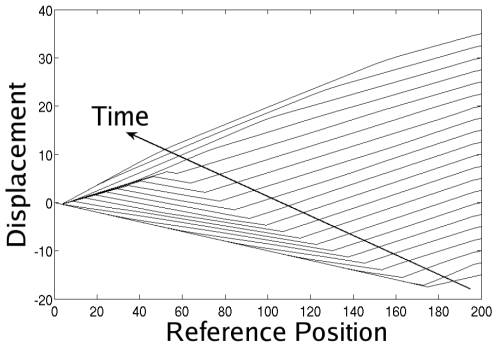

(d) Moderate velocity, viscous

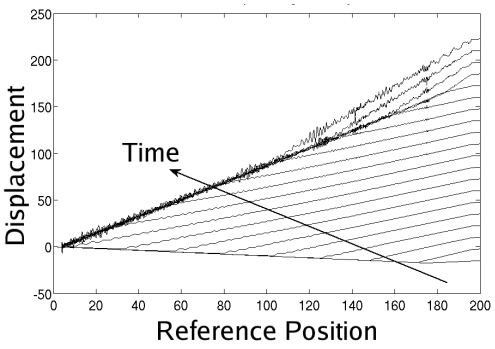

(e) High velocity, inviscid

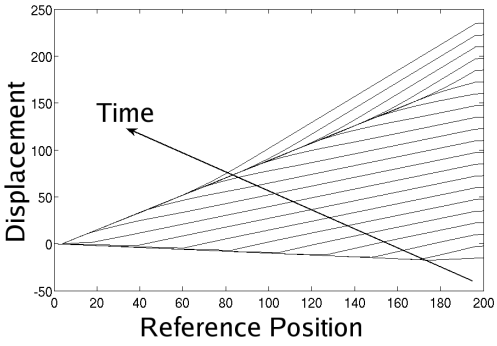

(f) High velocity, viscous

Figure 2.5: Snapshots of the displacement field in the impact problem with initial phase boundary.

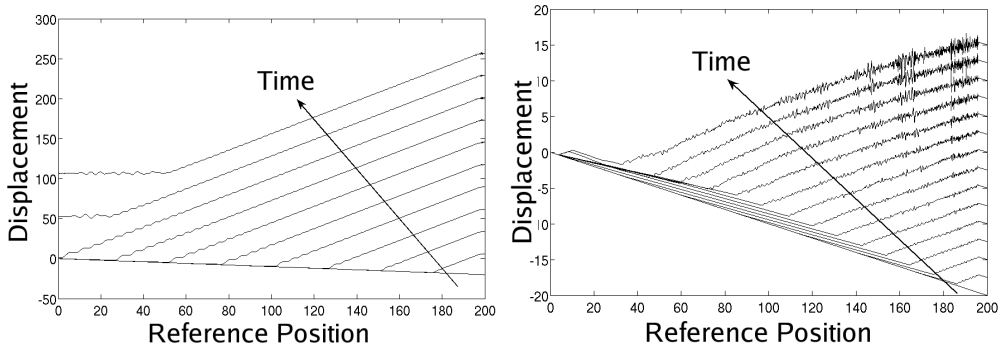

(a) Stress control (b) Displacement control

Figure 2.6: Snapshots of the displacement field in the inviscid impact problem without initial phase boundary.

again leaving the entire bar in the high strain state.

As in the release problem, viscosity plays a role in removing the short wavelength oscillations without changing the kinetics greatly.

Finally, the phase boundaries propagate steadily with fixed structure after an initial transient, and by plotting the driving force versus velocity in Figure 2.4, we see that they follow the same kinetic relation as the release problems.

2.4.3 Impact problem without initial phase boundary

We finally turn to impact problems with initial conditions involving a uniform strain field. We set the strain equal to the low-strain equilibrium value in the entire bar. We find that weak impact results in just an acoustic wave traveling into the bar, but a sufficiently strong impact causes the nucleation of a phase boundary at the impacted end. The displacement fields for impact experiments with different boundary conditions is shown in Figure 2.6.

Figure 2.6(a) shows an inviscid bar completely in the low strain phase, subjected to a tensile stress (soft loading) at the right end and left free at the left end. The tensile stress is applied as a step loading, and this causes an acoustic wave and a phase boundary to nucleate at the shocked end. The acoustic wave travels faster than the phase boundary till it reaches the far free end, and bounces off without nucleating

any new phase boundary.

Figure 2.6(b) shows an inviscid bar completely in the low strain phase, subjected to a displacement controlled extension with the far end clamped. We see, as before, that an acoustic wave and a phase boundary are nucleated at the impact side of the bar. The acoustic wave nucleates an additional phase boundary when it bounces off the far end that is clamped, in contrast to the previous case where no nucleation occurred at the free end.

We explain the reason for the different nucleation behavior under different clamping conditions in Section 2.5 after we formulate a nucleation criterion.

2.5 Nucleation as a dynamic instability

The numerical experiments in the previous sections show that nucleation occurs naturally from within the peridynamic theory. Further, the nucleation behavior is varied but very important in determining the overall behavior; recall the contrast between the hard and soft loading or the difference between the clamped and free end. We therefore seek to understand the conditions under which nucleation occurs by examining the point of view that nucleation occurs as a result of a dynamic instability.

We study the nucleation of the high strain phase from the low strain phase and note that the reverse transformation is completely analogous. Further, we modify the constitutive relation (2.4) slightly by translating the strain axis so that the boundary between the low strain and unstable branches occurs at $\frac{\epsilon_0}{2}$ (instead of at $-\frac{\epsilon_0}{2}$). We note that this modification is simply a change of variables for convenience and does not affect any results. Finally, we only consider the low strain and unstable branches, because we are only interested in the rate of growth of a perturbation from the low strain phase for small times.

While our numerical calculations involved finite slabs, the lengths of the slabs were much larger than the intrinsic peridynamic interaction length. For the analysis in this section, we treat the slabs as being of infinite length.

Consider a displacement field $u(x,t)$ evolving according to the peridynamic equa-

tion of motion. It is easy to verify that this solution remains linearly stable as long as all springs remain in the low strain region. So, let us consider a time when most springs are in the low strain region but some springs have reached beyond the limit and into the unstable region. We call such a displacement field a *defect*, and examine its linear stability. We call it a *stable defect* if it is linearly stable and an *unstable defect* if it is linearly unstable. Note that all defects - stable and unstable - contain some springs that are in the unstable region. However, stable defects are stable despite that. We postulate that unstable defects lead to nucleation.

We perturb the displacement field $u(x,t) \mapsto u(x,t) + \epsilon v(x,t)$ and study the evolution of this perturbed field. Substituting this in the governing equation (2.2) and differentiating with respect to ϵ gives us the linearized equation in $v(x,t)$

$$\partial_{tt} v(x,t) = \int_{\mathbb{R}} f_{,1}(u(x',t) - u(x,t), x' - x)\ (v(x',t) - v(x,t))\ dx' \tag{2.9}$$

where $f_{,1}(u(x',t) - u(x,t), x' - x)$ is the derivative of $f(\cdot,\cdot)$ with respect to the first argument and evaluated at $(u(x',t) - u(x,t), x' - x)$. For conciseness, we denote $f_{,1}(u(x',t) - u(x,t), x' - x)$ by $C_u(x,x')$, and we note that $C_u(x,x') = \pm e^{-(x'-x)^2}$ with the plus sign for stable springs and the minus sign for unstable springs.

By separation of variables we find that $v(x,t) = v(x)e^{i\omega t}$ where ω and $v(x)$ are given by the following eigenvalue problem:

$$\omega^2 v(x) = \int_{\mathbb{R}} C_u(x,x')\,(v(x) - v(x'))\ dx' =: L_u[v(x)]. \tag{2.10}$$

If ω is real or if it contains only positive imaginary part, then the solution u is stable. The solution is unstable if it has a negative imaginary part.

It is easy to verify using standard methods in integral equations (see, for example, Porter and Stirling, 1990) that the operator L_u is self-adjoint in the Hilbert space of locally square integrable functions. It follows that all its eigenvalues ω^2 are real. Therefore, the stability of the solution u reduces to examining the smallest eigenvalue of L_u: the solution u is unstable if the smallest eigenvalue is negative and stable

otherwise. Further, the smallest eigenvalue can be posed as a variational problem of finding the minimum of

$$I(v) = \int_{\mathbb{R}^2} C_u(x, x') \left(v(x)^2 - v(x')v(x) \right) \, dx' \, dx \tag{2.11}$$

over all functions v with

$$\int_{\mathbb{R}} v^2 dx = 1. \tag{2.12}$$

To evaluate the functional I above, it is important to identify which springs are in the stable phase and which are not. This is not straightforward to identify for an arbitrary displacement field $u(x)$, since this depends on the displacement of two distant points that are connected by the spring. So, it is natural to work in the two-dimensional space x vs. x' shown in Figure 2.7(b). We divide this space into stable and unstable regions: a point (x, x') is in the stable region if the spring connecting x and x' is stable, and in the unstable region otherwise. Assuming that the unstable regions are localized, we have the picture shown in Figure 2.7(b) based on two lengthscales: a lower lengthscale δ^l such that all springs with both $|x| < \delta^l, |x'| < \delta^l$ are unstable and $C_u(x, x') = -e^{-(x'-x)^2}$, and an upper lengthscale δ^u such that all springs with either of $|x|, |x'| > \delta^u$ are stable and $C_u(x, x') = e^{-(x'-x)^2}$. The values of δ^l, δ^u and hence the sizes of the different regions in the spring-space will depend on the shape of the defect.

We begin our consideration with a special displacement field $u(x)$ that we call the *ideal defect* where $\delta^l = \delta^u = \delta$. This displacement field is shown in Figure 2.7(a), with slope $u'(x) \leq \frac{\epsilon_0}{2}$ for $|x| > \delta$, and a uniform slope $u'(x) = \frac{\epsilon_0}{2}$ for $|x| < \delta$. In other words, we are in the stable low strain phase except for an interval of length 2δ, where we are at the limiting strain that separates the low strain from the unstable phase. We examine the stability of the ideal defect and then use it to obtain bounds on the the behavior of a general displacement field.

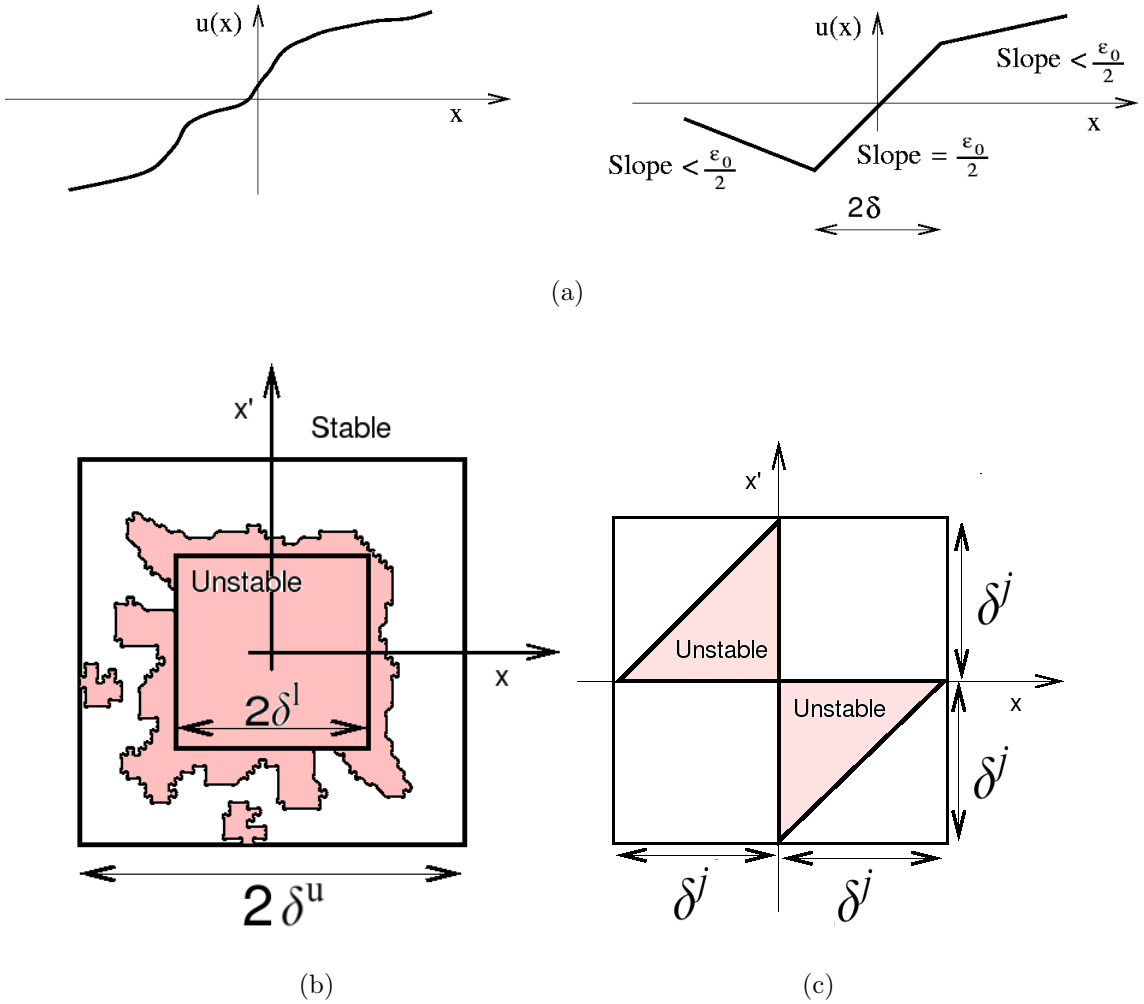

Figure 2.7: Defect geometries and spring space maps. (a) The displacement fields of a typical and ideal defect, (b) The two-dimensional spring-space associated with typical defects. The springs connecting (x, x') in the shaded region are unstable and the others are stable. (c) The two-dimensional space associated with a jump defect.

The linear operator associated with the ideal defect is

$$\begin{aligned} L_\delta[v(x)] := & \int_{\mathbb{R}} e^{-(x'-x)^2} \left(v(x) - v(x')\right)\ dx' \\ + \quad & 2H(\delta - |x|) \left(-v(x) \int_{(-\delta,\delta)} e^{-(x'-x)^2}\ dx' + \int_{(-\delta,\delta)} e^{-(x'-x)^2} v(x')\ dx' \right) \end{aligned}$$

where $H(y)$ is the unit Heaviside step function that is 0 for $y < 0$ and 1 for $y > 0$ and the functional (2.11) becomes

$$\begin{aligned} I_\delta(v) = & \int_{\mathbb{R}^2} e^{-(x'-x)^2} \left(v(x)^2 - v(x)v(x')\right)\ dx\ dx' \\ - \quad & 2 \int_{(-\delta,\delta)^2} e^{-(x'-x)^2} \left(v(x)^2 - v(x)v(x')\right)\ dx\ dx' \end{aligned} \tag{2.13}$$

By setting $\delta = 0$, we see that $I_0 > 0$. Further, one can use Fourier analysis to show that the minimum of I_δ is continuous with respect to δ at $\delta = 0$. So, we expect the ideal defect to be stable for small δ. Further, setting $\delta \to \infty$, we see that $I_\infty < 0$. Therefore, we anticipate that the ideal defect becomes unstable beyond some finite δ.

To understand this further, we examine (2.13) above for a finite δ. We expect the minimum to be achieved for functions v that are strongly localized near the origin so that the second term dominates. Physically, we are exciting primarily the unstable springs near the origin while exciting as few stable springs as possible. For such a function,

$$\begin{aligned} I_\delta(v) \quad = \quad & \pi^{\frac{1}{2}} + \int_{(-\delta,\delta)^2} e^{-(x'-x)^2} v(x)v(x')\ dx\ dx' \\ & -\pi^{\frac{1}{2}} \int_{(-\delta,\delta)} \left(\operatorname{erf}(x+\delta) - \operatorname{erf}(x-\delta)\right) v(x)^2\ dx \\ \approx \quad & \pi^{\frac{1}{2}} + \int_{(-\delta,\delta)^2} v(x)v(x')\ dx\ dx' - 2\pi^{\frac{1}{2}} \operatorname{erf}(\delta) \int_{(-\delta,\delta)} v(x)^2\ dx \end{aligned}$$

by approximating the values of the integrands near $x = 0, x' = 0$. Using the fact that the double integral above is now decoupled into 2 single integrals that are equal, we can write the double integral as a square, and hence it is positive. Since v is localized, we can extend the range of integration in the second integral to all space, and then

use (2.12) to conclude that this second integral is equal to one. Therefore,

$$\begin{aligned} I_\delta(v) &\geq \pi^{\frac{1}{2}} \left(1 - 2\,\mathrm{erf}(\delta)\right) \\ &\geq 0 \quad \text{if} \quad \mathrm{erf}(\delta) \leq \frac{1}{2} \Leftrightarrow \delta \lesssim 0.477 \end{aligned} \tag{2.14}$$

This provides an upper bound for the size of a stable ideal defect. Numerical computations below show that this bound is, in fact, attained. Thus, we conclude that the ideal defect is stable if $\delta \leq \mathrm{erf}^{-1}\,\frac{1}{2} \approx 0.477$ and unstable for larger δ.

For the numerical computations, we consider an infinite bar and discretize the operator L_δ as

$$\begin{aligned} (L_\delta)_{ij} = \quad & \delta_{ij}\pi^{\frac{1}{2}} \left(1 + H(\delta - |x_i|) \left(\mathrm{erf}(x_i - \delta) - \mathrm{erf}(x_i + \delta)\right)\right) \\ - \quad & e^{-(x_i - x_j)^2}\Delta x + 2H(\delta - |x_i|)H(\delta - |x_j|)e^{-(x_i - x_j)^2}\Delta x \end{aligned} \tag{2.15}$$

and use standard numerical algorithms (Anderson et al., 1999) to find the smallest eigenvalue. Notice that zero is always an eigenvalue for the original (continuous) operator with rigid translation as the eigenmode. While rigid translation is not square-integrable on infinite domains, it alerts us to the fact that the infimum of the spectrum may in fact be zero. Therefore, we look for eigenmodes with finite support, and the results are plotted in Figure 2.8 where the support of v is limited to the intervals $(-100, 100)$, $(-10, 10)$, $(-5, 5)$, $(-3, 3)$, $(-1, 1)$, $(-0.5, 0.5)$ and $(-0.1, 0.1)$. For small defect size δ, the smallest eigenvalue is positive (with the value depending on the support of v) and remains constant[2] with δ. We have found that the eigenmode associated with this eigenvalue is an approximation to the rigid translation mode of the original (continuous) operator. This remains the smallest eigenvalue with increasing defect size δ till a critical value where it crosses the eigenvalue associated with what eventually becomes the localized unstable mode. The eigenvalue associated with this mode is monotone decreasing with δ, insensitive to the constraint on the support of v, follows closely the analytic predictions above and becomes negative at $\delta \approx 0.477$.

[2]The small oscillations are discretization artifacts and we have verified that they go away with refinement.

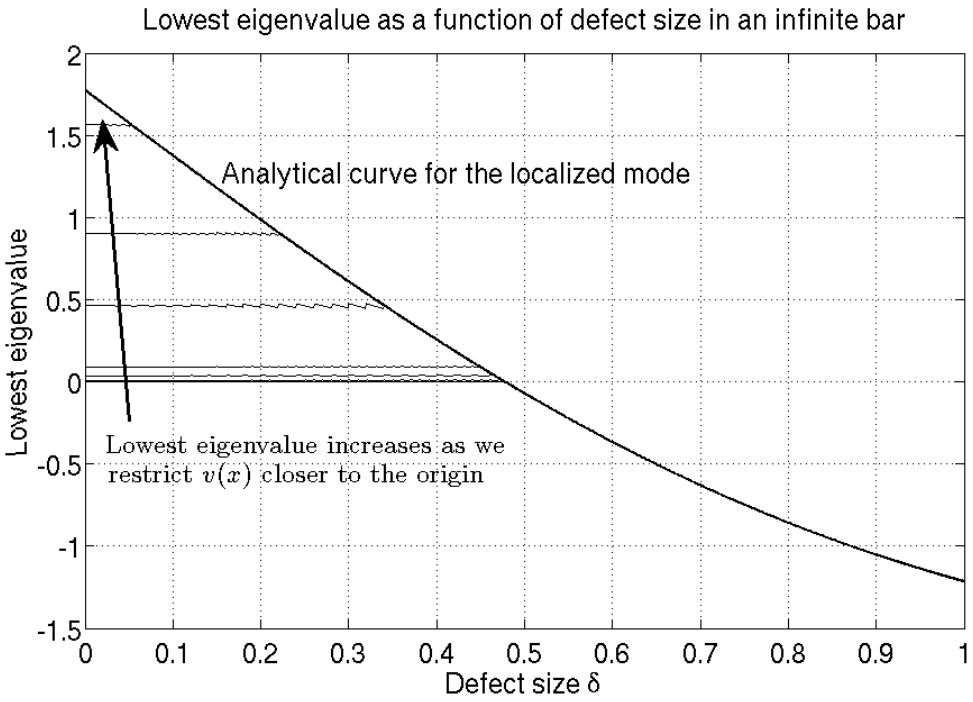

Figure 2.8: Numerical calculation of the lowest eigenvalue

We have obtained similar results with a second discretization based on a bar of finite length; the lowest eigenvalue is zero with rigid body eigenmode until the localized mode becomes unstable.

We now turn to the general defect. We show in Appendix 2.A that the results above for the ideal defect can be used to obtain bounds on the stability of any general defect with radii δ^l, δ^u. If follows that any defect is stable if $\text{erf}(\delta^u) < \frac{1}{2}$ and any defect is unstable if $\text{erf}(\delta^l) > \frac{1}{2}$.

Finally, we turn to a defect that consists of a displacement jump. The solutions of the peridynamic equations may contain a displacement discontinuity, for example when the initial displacement, initial velocity or applied body force contain such a discontinuity (Weckner and Abeyaratne, 2005). In fact, we encountered such discontinuities in our numerical experiments earlier.

Consider a displacement field with uniform strain $\bar{\epsilon}(< \epsilon_0/2)$ with a jump discontinuity at the origin. It is easy to find the stable and unstable springs, and this is

shown in Figure 2.7(c) with

$$\delta^u = \delta^j = \frac{[\![u]\!]}{\Delta\epsilon} \qquad \delta^l = 0. \tag{2.16}$$

where $\Delta\epsilon = \epsilon_0/2 - \bar{\epsilon}$. Since $\delta^l = 0$, we can not directly apply the bounds in Appendix 2.A. We instead study it numerically to find the critical value of δ^j (≈ 0.75) below which the jump defect is stable and beyond which it is unstable.

Equation (2.16) reveals an important scaling property of peridynamics. It shows that the defect size depends on how far the ambient strain field is from the critical strain ($\Delta\epsilon$). We show in Appendix 2.B that this is not the case in the traditional regularized theories.

With the stability results in hand, we consider a series of dynamic calculations using the original constitutive relation (2.4) to probe the applicability of these stability considerations to nucleation in fully nonlinear calculations. The first set of calculations consists of initial condition with a bar with uniform strain in the low strain phase and with a single displacement continuity. We consider various initial strains and jumps and catalog when they lead to nucleation and when they do not. We find that there is no nucleation when the initial defect size $\frac{[\![u]\!]}{\Delta\epsilon}$ is smaller than 1.0, but nucleation whenever it exceeds it. This confirms the scaling predicted by linear stability considerations, though the critical value is larger than predicted. The second set of calculations consist of initial conditions with uniform strain but discontinuous velocity. Once again, we vary the initial strain and velocity jump and catalog when they lead to nucleation and when they do not. These calculations again confirm the scaling predicted by the stability criterion, though the critical defect size is 0.42.

The third and final set of calculations consists of initial conditions with uniform strain but subjected to discontinuous body force. Repeating the calculations for various initial strains and body force jumps, we again find that the scaling agrees very well. We note that in this case, nucleation does not depend only on the size of the discontinuity in the body force, but also the extent of the region over which the body force is applied (as this is related to the total force applied on the body and

strongly influences the evolution of the surrounding strain field). For a few different sizes of region of application (with the body force being constant within these regions), we obtain the same scaling with initial strain field, but of course the size of the critical defect varies depending on the size of the application region.

In summary, we find that the stability calculations correctly identify the defect size to be the entity which determines nucleation. However, the value of the critical defect size may depend on the particular situation. One reason for this is that a displacement discontinuity in a peridynamic theory is fixed in space but evolves with time according to a simple second order equation (Weckner and Abeyaratne, 2005):

$$\frac{d^2}{dt^2}[\![u]\!] + \sqrt{\pi}[\![u]\!] = [\![b]\!] \tag{2.17}$$

Thus, if we start with a displacement discontinuity but no velocity discontinuity in the initial condition, the magnitude of the displacement discontinuity decreases with time before the instability has time to develop. Hence, we expect the stability criterion applied to the initial condition to over-predict nucleation as we find above. In contrast, when one has an initial velocity but no displacement discontinuity, the displacement discontinuity as well as the ambient strain grow with time and thus we anticipate our stability condition to under-predict the instability as we find above.

We conclude this section by revisiting the numerical experiments in the previous sections. In the quasistatic hard loading, each displacement increment gives rise to a displacement jump of $[\![u]\!] = 0.200$. We then expect nucleation to occur when the difference between the unstable strain and the ambient strain $\Delta\epsilon$ reaches $0.2/\delta^{crit}$. On the increasing half-cycle, this corresponds to a value of ambient strain smaller than $\epsilon = -0.25$, which is smaller than the smallest strain considered. So, we conclude that nucleation occurs at each displacement increment in that calculation. However, as long as we are below the Maxwell stress, we expect the newly nucleated phase boundaries to be driven out of the bar during the subsequent equilibration. Thus, we expect phase transformation to begin at the Maxwell stress, and this is exactly what we see in Figure 2.1. We have verified our argument by examining the transients in

our calculations. Further, these calculations show that we can control the point at which phase transformation begins by taking smaller displacement increments so as to create smaller displacement jumps; we have verified this numerically.

In the case of quasistatic soft loading, we note that nucleation occurs close to the peak but not exactly at the peak. If we compare the defect radius at the load step just before nucleation, and the point on the curve that the bar would reach had nucleation not taken place, we see that we obtain a critical nucleation outer radius between 0.505 and 0.530 in agreement with our earlier result.

In the impact problem without an existing phase boundary, recall that a new phase boundary was nucleated at the far end by the acoustic wave when that end is clamped but not when that end is free. With a clamped end, the impinging acoustic wave creates a velocity discontinuity that in turn leads to a displacement discontinuity and thus nucleation. In contrast, with a free end, there is no defect created and there is no nucleation.

In summary, we find that linear instability of the dynamic solution is an accurate predictor of nucleation.

2.6 Phase boundaries as traveling waves

A noticeable feature of the numerical solutions to dynamic problems that we obtain in Section 2.4 is that the phase boundaries appear to have an invariant shape and move at a constant velocity. Hence, we seek a solution to (2.2) in the form of a traveling wave,

$$u(x,t) = u(x - vt) \tag{2.18}$$

that connects the two phases. Substituting (2.18) in (2.2), the governing equation becomes[3]

$$\mathsf{M}^2 \left(\frac{d^2 u(y)}{dy^2} \right) = \left(\frac{1}{E} \int_0^L f(u(y') - u(y), y' - y) dy' \right) \tag{2.19}$$

[3]We have assumed that our computational window is translating with the phase boundary, and the limits of the integral are correspondingly changed.

where $\mathsf{M} = \frac{v}{c}$ and $y := x - vt$ is the coordinate in the translating frame that moves with the phase boundary at a constant velocity v. The second derivative on the left hand side would seem to impair the ability of peridynamics to be valid at all points in the body, including at singularities. However, we note the result of Weckner and Abeyaratne (2005) that a displacement or velocity discontinuity has a fixed position at all time. As we are working in a translating frame that moves with a constant velocity v, such discontinuities are not allowed to exist in $u(y)$, and we can define a weak second derivative.

The discretization in space is given by:

$$\int_0^L f(u(x',t) - u(x_j,t), x' - x_j)dx' \approx \sum_{i=1}^{N} f(u_i(t) - u_j(t), x_i - x_j)\Delta x \tag{2.20a}$$

$$\frac{d^2u(y)}{dy^2} \approx \frac{u_{j+1} - 2u_j + u_{j-1}}{(\Delta y)^2} \tag{2.20b}$$

and we have used $\Delta x = 0.1$ as before.

We now attempt to solve the traveling wave problem by assuming a value for M and finding the associated displacement field. From the displacement field, we can find the strain field and hence the driving force associated with this M.

To find the displacement field, we divide the domain $\mathcal{R} := \{y : y \in [0, L]\}$ into an interior $\mathcal{I} := \{y : y \in [L_{bc}, L - L_{bc}]\}$, a left boundary layer $\mathcal{B}_- := \{y : y \in [0, L_{bc}]\}$, and a right boundary layer $\mathcal{B}_+ := \{y : y \in [L - L_{bc}, L]\}$. We define the residue $R(u(y)) := \left[\mathsf{M}^2\left(\frac{d^2u(y)}{dy^2}\right) - \left(\frac{1}{E}\int_0^L f(u(y') - u(y), y' - y)dy'\right)\right]$. We aim to minimize the 2-norm of the residue over the interior $\mathcal{I}$:

$$\min \int_{\mathcal{I}} R(u(y))^2 \, dy \approx \min \sum_{u(y_i)\in\mathcal{I}} R(u(y_i))^2 \tag{2.21}$$

Our initial approach was to minimize the norm of the residual (normalized with respect to the height of the energy barrier and length of the computational domain) on $\mathcal{I}$ over the set of displacements $u(y_i)$ where $y_i \in \mathcal{I}$ and assuming constant strain fields in $\mathcal{B}_-, \mathcal{B}_+$ by extrapolating. As M increases, the constant strain approximation

does not work. Instead, we minimize the norm of the residual on $\mathcal{I}$ over the entire set of displacements $u(y_i)$ where $y_i \in \mathcal{B}_- \cup \mathcal{I} \cup \mathcal{B}_+$. This allows us to capture the oscillations around the phase boundary. A singularity is formed at the interface of the boundary layer with the interior, and is analogous to the singularity expected when the applied body force changes sharply in space (Silling et al., 2003), if we think of the error minimization process in terms of a fictitious body force applied in the boundary layers.

The minimization is performed using a standard conjugate gradient algorithm (Anderson et al., 1999). We start with a static phase boundary (i.e., $\mathsf{M} = 0$), and use this as the initial guess for a phase boundary moving at a low M. Once we have found this phase boundary, it is then used as an initial guess for a slightly faster phase boundary. This procedure is repeated till we come as close to $\mathsf{M} = 1$ as possible. For phase boundaries that are very close to $\mathsf{M} = 1$, the conjugate gradient solver is unable to find a solution that connects the two phases and instead finds solutions that are single-phase.

With viscosity ($\nu = 0.333$), the traveling wave calculations yield the kinetic relation shown as the dashed line in Figure 2.4. It coincides with that obtained from dynamic calculations with the same value of viscosity in the previous section. A typical traveling wave profile (at $\mathsf{M} = 0.33$) is shown in Figure 2.9(a).

For the inviscid material, however, the situation is different. We still obtain traveling waves, but the displacement field is quite different from those observed in dynamic calculations. One has sinusoidal waves of a specific frequency that do not die out but persist over all space with constant amplitude, as shown in Figure 2.9(b). Similar solutions have been found by Zimmermann (2002). Further, they are symmetric, i.e., the strain fields on either side of the phase boundary are reflections of each other around the zero-strain line. Consequently, it follows from (2.8) that the driving force is zero. Thus, the kinetic relation is a horizontal line $F = 0$, again differing from the dynamic calculations.

To explore this issue further, we break the symmetry of the displacement field for an inviscid phase boundary by adding viscosity, and study the limiting kinetic

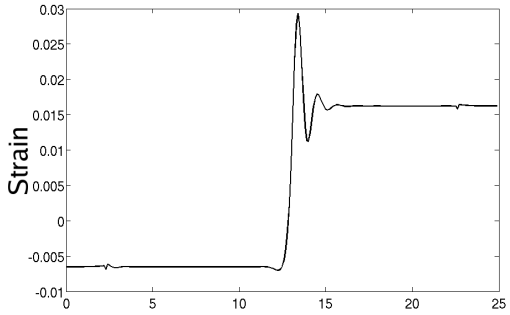

(a) Viscous ($\nu = 0.333$)

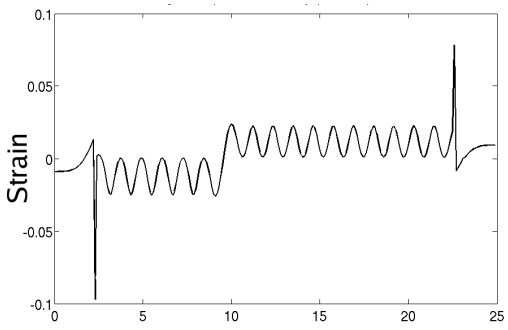

(b) Inviscid

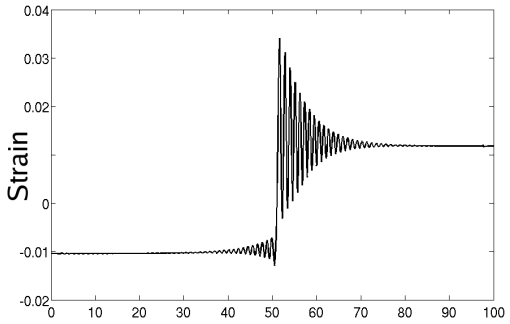

(c) Almost inviscid ($\nu = 0.005$)

Figure 2.9: Strain fields from the traveling wave calculations at $\mathsf{M} = 0.33$. Note the different scales.

relation as $\nu \to 0$. The entire calculation (going from $\mathsf{M} = 0$ to $\mathsf{M} \simeq 1$) is repeated for different values of ν. A typical traveling wave profile ($\mathsf{M} = 0.33$) for small viscosity ($\nu = 0.005$) is shown in Figure 2.9(c). The kinetic relation converges to the solid line shown in Figure 2.4, which is identical to that derived from inviscid dynamics simulations earlier. We speculate that the numerical damping inherent in our time marching discretization picks the limiting (rather than the exact) inviscid solutions in our dynamic simulations.

The numerical computations above suggest that the inviscid limit is discontinuous: the limit of the viscous solutions as $\nu \to 0$ differs non-trivially from the solution obtained by setting $\nu = 0$. We speculate briefly on the physical origins of this difference. Recall that when the viscosity is zero, the traveling wave consists of strain oscillations in all space in the traveling frame. These oscillations imply a velocity difference between every pair of points. Thus, the addition of even a small ν would lead to infinitely large dissipation and consequently an infinitely large driving force to sustain this structure. Therefore, one would expect that the oscillations to decay with the slightest addition of viscosity thereby leading to a very different solution.

We now examine this discontinuous limit mathematically. Let $u_0(y)$ be the inviscid solution, and $u(y)$ be the solution with viscosity. These solutions satisfy the equations

$$F(u_0) - \mathsf{M}^2 \left(\frac{d^2 u_0(y)}{dy^2} \right) = 0, \tag{2.22a}$$

$$F(u) - \nu \mathsf{M} \int \left(\frac{du(y')}{dy'} - \frac{du(y)}{dy} \right) e^{-(y'-y)^2} dy' - \mathsf{M}^2 \left(\frac{d^2 u(y)}{dy^2} \right) = 0 \tag{2.22b}$$

where $F(\cdot)$ represents the nonlinear functional containing the elastic peridynamic interactions. We subtract the equations and linearize $F(u)$ about the inviscid solution to obtain:

$$T_{u_0} U(y) = \nu \mathsf{M} \int \left(\frac{du(y')}{dy'} - \frac{du(y)}{dy} \right) e^{-(y'-y)^2} dy' \tag{2.23}$$

where $U(y) := u(y) - u_0(y)$ and

$$T_{u_0}U(y) := \int_{\mathbb{R}} K(y,y')\left(U(y') - U(y)\right) e^{-(y'-y)^2} dy' - \mathsf{M}^2 \left(\frac{d^2U(y)}{dy^2}\right) \tag{2.24}$$

and $K(y,y')$ is the indicator function that is $+1$ when it connects a stable spring, and -1 when it connects an unstable spring.

As $\nu \to 0$, the right-hand-side of (2.23) approaches zero. This would imply that U approaches zero if the spectrum of T_{u_0} is bounded away from zero. If, however, zero is either in the spectrum or an accumulation point of the spectrum of T_{u_0}, then (2.23) is ill-posed and one can have non-trivial solutions solutions for U (see, for example, Engl et al., 2000). We shall now show that we are in this latter situation.

To understand the spectrum of T_{u_0}, we have to first characterize $K(y,y')$. This can be quite complicated as we discussed in the previous section depending on the state about which we linearize. Note that if $K(y,y') = -1$ (respectively $K(y,y') = +1$) everywhere, then the spectrum is given by $-\pi^{\frac{1}{2}}\left(1 - e^{-k^2/4}\right) + \mathsf{M}^2k^2$ (respectively $\pi^{\frac{1}{2}}\left(1 - e^{-k^2/4}\right) + \mathsf{M}^2k^2$). Clearly, 0 is an accumulation point of the spectrum in both these cases.

To study the general case, we verify that the operator T_{u_0} is self-adjoint and thus the spectrum is bounded from above and below by the minimum and maximum values of

$$\begin{aligned}
&\langle U(y), T_{u_0}U(y)\rangle \\
&= \frac{1}{2}\int_{\mathbb{R}^2} K(y,y')\left(U(y') - U(y)\right)^2 e^{-(y'-y)^2} dy'dy - \mathsf{M}^2 \int_{\mathbb{R}} \left(\frac{d^2U(y)}{dy^2}\right) U(y)dy \\
&= \frac{1}{2}\int_{\mathbb{R}^2} \left(U(y') - U(y)\right)^2 e^{-(y'-y)^2} dy'dy - \mathsf{M}^2 \int_{\mathbb{R}} \left(\frac{d^2U(y)}{dy^2}\right) U(y)dy \\
&\qquad -\frac{1}{2}\int_{\mathbb{R}^2} \left(1 - K(y,y')\right)\left(U(y') - U(y)\right)^2 e^{-(y'-y)^2} dy'dy \\
&= -\frac{1}{2}\int_{\mathbb{R}^2} \left(U(y') - U(y)\right)^2 e^{-(y'-y)^2} dy'dy - \mathsf{M}^2 \int_{\mathbb{R}} \left(\frac{d^2U(y)}{dy^2}\right) U(y)dy \\
&\qquad +\frac{1}{2}\int_{\mathbb{R}^2} \left(1 + K(y,y')\right)\left(U(y') - U(y)\right)^2 e^{-(y'-y)^2} dy'dy
\end{aligned} \tag{2.25}$$

over all appropriately normalized U where $\langle \cdot, \cdot \rangle$ denotes the inner product and we have used (2.32). The integrals above containing the terms $1 - K(y, y')$ and $1 + K(y, y')$ are always positive. The remaining terms correspond to the cases considered above where $K = 1$ or $K = -1$ everywhere. It follows then that 0 is either an accumulation point of the spectrum or is contained in the spectrum for any spatial variation of $K(y, y')$.

2.7 Interaction of a phase boundary with an inclusion in two dimensions

In this section, we study the problem of a phase boundary, separating two variants of martensite, impinging on an isolated elastic (non-transforming) defect in two dimensions.

We model a material undergoing a square to rectangle phase transformation in two dimensions by using an energy that has two minima that are related by square symmetry. As shown schematically in Figure 2.10(a), we use trilinear springs in the $\mathbf{e_1} = \begin{pmatrix} 1 \\ 0 \end{pmatrix}$ and $\mathbf{e_2} = \begin{pmatrix} 0 \\ 1 \end{pmatrix}$ directions and we add linear springs in the $\frac{\mathbf{e_1}+\mathbf{e_2}}{\sqrt{\mathbf{2}}}$ direction to prevent both springs simultaneously being in the low- or high-strain phase. We smooth the angular dependence by multiplying by a sinusoidal function. Putting all these together, we arrive at the following constitutive relation:

$$\mathbf{f}(\delta\mathbf{u}, \delta\mathbf{x}) = \left(f_2(\lambda)\cos^2(2\phi) + f_1(\lambda)\sin^2(2\phi)\right)\frac{\delta\mathbf{x} + \delta\mathbf{u}}{|\delta\mathbf{x} + \delta\mathbf{u}|}e^{-|\delta\mathbf{x}|^2} \tag{2.26}$$

where $\lambda := \frac{|\delta\mathbf{x}+\delta\mathbf{u}|}{|\delta\mathbf{x}|} - 1$, $\tan\phi := \frac{\delta x_2}{\delta x_1}$ and the functions f_1, f_2 are the 1-well and 2-well springs:

$$f_1 = 2\lambda \tag{2.27a}$$

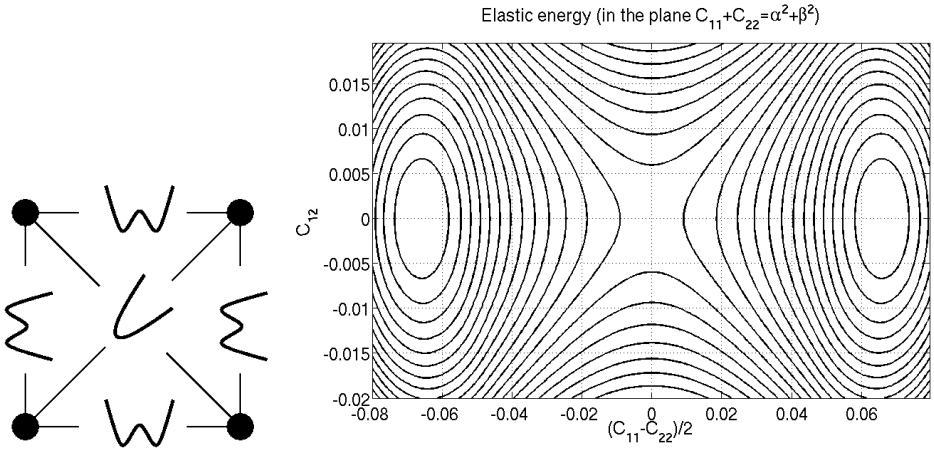

(a) Unit cell (b) Energy density

Figure 2.10: Model of a two-well material in peridynamics. (a) The unit cell consists of one and two-well springs. (b) The level sets of the energy density show two wells.

$$f_2 = \begin{cases} \lambda - 0.1 & \text{if } \lambda > 0.05 \\ -\lambda & \text{if } -0.05 < \lambda < 0.05 \\ \lambda + 0.1 & \text{if } \lambda < -0.05 \end{cases} . \tag{2.27b}$$

Figure 2.10(b) shows the level sets of the macroscopic energy density when the material is subjected to a homogeneous deformation $\mathbf{y} = \mathbf{F}\mathbf{x}$. It is plotted as a function of $C_{11} - C_{22}$ and C_{12} with $C_{11} + C_{22}$ held fixed, where $\mathbf{C} = \mathbf{F}^{\mathbf{T}}\mathbf{F}$. The energy has two wells at

$$\mathbf{U}_1 = \begin{pmatrix} \alpha & 0 \\ 0 & \beta \end{pmatrix} \qquad \mathbf{U}_2 = \begin{pmatrix} \beta & 0 \\ 0 & \alpha \end{pmatrix} \tag{2.28}$$

where $\alpha = 1 + 0.0645, \beta = 1 - 0.0730$ for the particular choice of parameters.

The inclusion is modeled after a non-transforming elastic material. Therefore, the constitutive relation in this region is chosen to be

$$\mathbf{f}(\delta\mathbf{u}, \delta\mathbf{x}) = \left(\lambda \cos^2(2\phi) + 2\lambda \sin^2(2\phi)\right) \frac{\delta\mathbf{x} + \delta\mathbf{u}}{|\delta\mathbf{x} + \delta\mathbf{u}|} e^{-|\delta\mathbf{x}|^2} \tag{2.29}$$

where ϕ, λ are as defined earlier. The macroscopic energy density of this material has a single well at the identity. We also choose this same constitutive relation for springs

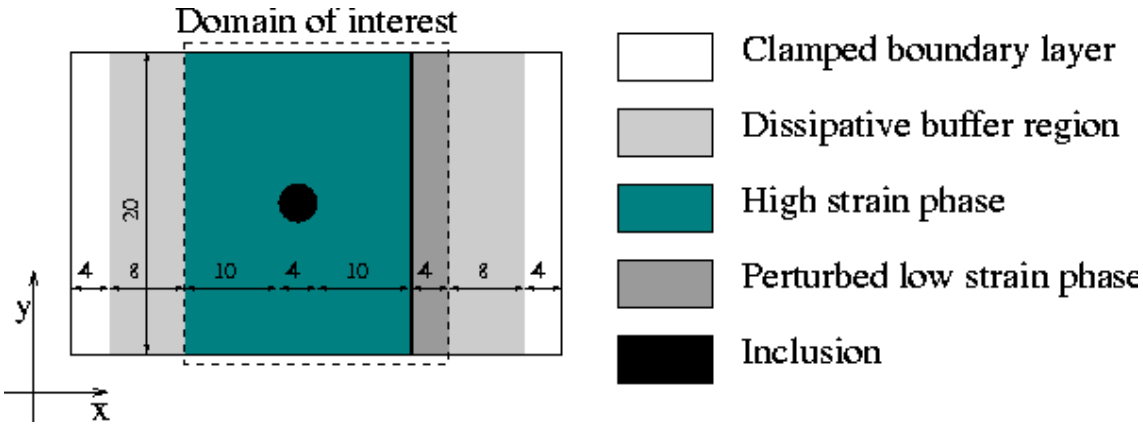

Figure 2.11: Initial and boundary conditions for the 2 dimensional dynamic calculation

connecting pairs of points that have one point in the inclusion and the other in the martensite.

We recall from the classical theory of martensites (see, for example, Bhattacharya, 2003) that two wells with transformation matrices given by (2.28) are in fact compatible, i.e., we can find a rotation matrix $\mathbf{Q}$ and vectors $\mathbf{a}, \hat{\mathbf{n}}$ such that

$$\mathbf{Q}\mathbf{U}_2 - \mathbf{U}_1 = \mathbf{a} \otimes \hat{\mathbf{n}}, \tag{2.30}$$

and thus, a material with these wells can form phase (or twin) boundaries with normal $\hat{\mathbf{n}}$ in the reference configuration. For the matrices given by (2.28), $\hat{\mathbf{n}} = \frac{\mathbf{e_1} \pm \mathbf{e_2}}{\sqrt{2}}$. For this reason, it is convenient to work in an orthonormal coordinate system aligned with the twin boundaries, $\mathbf{e_x} = \frac{\mathbf{e_1}+\mathbf{e_2}}{\sqrt{2}}, \mathbf{e_y} = \frac{\mathbf{e_1}-\mathbf{e_2}}{\sqrt{2}}$.

We seek to study the propagation of a phase boundary and its interaction with a non-transforming precipitate. Therefore, we consider a rectangular region marked in Figure 2.11 with a dashed line as the domain of interest. We use periodic boundary conditions in the y direction. We seek to simulate infinite length in the x direction with fixed far field strain. Therefore, we pad the domain of interest with dissipative buffer regions to prevent reflection of acoustic waves and clamp the far ends. Preventing reflection through the use of dissipative boundary layers increases the length of time that the system can be evolved to get usable results. The dissipation is linear in the velocity difference as in the one-dimensional calculation, and the coefficient of

viscous damping is gradually increased in the dissipative regions, as a sudden change in material properties would cause reflections at the interface of the damped and undamped regions.

We study a problem similar to the release problem in Section 2.4. We place a single phase boundary as shown in Figure 2.11 and equilibrate the system. The equilibrium state has significant residual stress because of the non-transforming inclusion, since its energy well is different from either of the phases and the circular boundary has both compatible and incompatible directions. The residual stress dies out quickly away from the inclusion and is not significant at the initial phase boundary. We now perturb the martensite on the right side of the phase boundary, by changing the displacement gradient $F_{i1} \mapsto (1+\epsilon)F_{i1}$. This perturbation maintains the continuity of the displacement field in the y-direction. Also, as the perturbation is uniform in the y-direction, the driving force is constant at all points along the phase boundary and the phase boundary remains straight until it interacts with the stress field caused by the inclusion. With these initial and boundary conditions, we integrate the peridynamic equation of motion (2.1) in time and examine the evolution of the displacement fields.

The mechanism that the phase boundary uses to move past the inclusion is interesting. Figure 2.12 shows snapshots of the deformation field[4] C_{22} at different times. The phases can be easily differentiated on the basis of high and low values of C_{22}. The inclusion is the prominent circular region in the center of the viewing area with a moderate value of C_{22}. As the phase boundary begins to move toward the inclusion, it also sends off acoustic waves that go ahead of it. When these acoustic waves hit the inclusion, they interact with the stress field and nucleate phase boundaries there that lead to a region of the low strain phase in the neighborhood of the inclusion. This low strain region near the inclusion then grows toward the left and consumes the high strain region beyond. The original phase boundary stops some distance away, leaving a remnant of untransformed high strain martensite partially surrounding the inclusion.

[4]While all calculations in the peridynamic theory involve only the displacement field and not its derivatives, we calculate $\mathbf{C}$ as a post-processing step to aid visualization of the results.

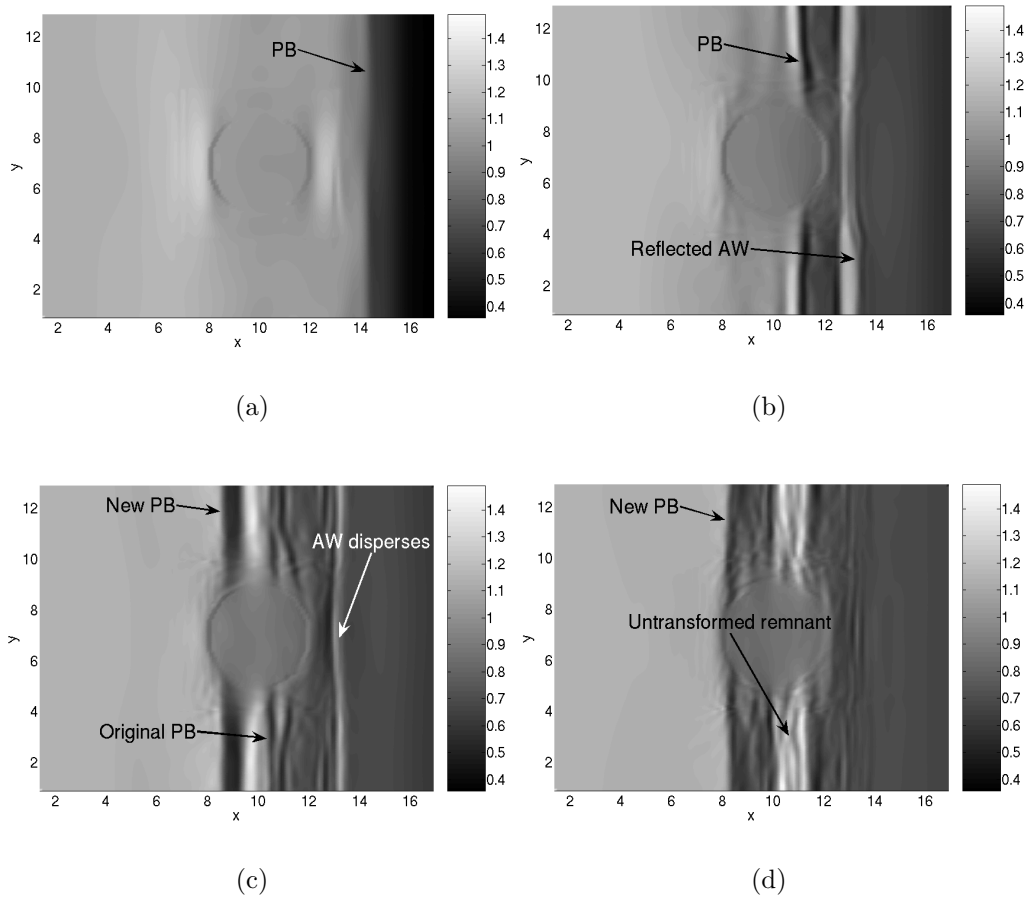

(a) (b)

(c) (d)

Figure 2.12: Interaction of the phase boundary with the inclusion at moderate velocities visualized through a plot of C_{22}. We have used PB to label phase boundaries, and AW to label acoustic waves. (a) Phase boundary approaching the inclusion, (b) Phase boundary hitting inclusion and acoustic wave reflected, (c) New phase boundary nucleates and original phase boundary stops, while acoustic wave disperses and (d) Nucleated phase boundary continues moving, leaving behind remnant of untransformed martensite.

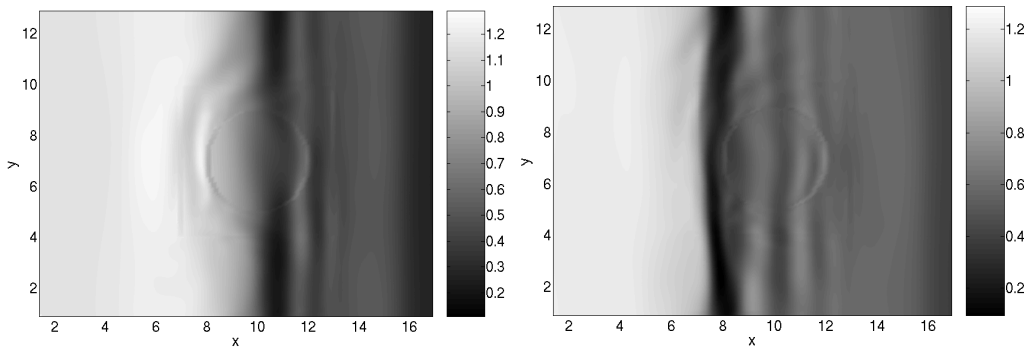

(a) (b)

Figure 2.13: Interaction of the phase boundary with the inclusion at large velocities visualized through a plot of C_{22}. (a) Phase boundary moving over the inclusion and (b) Phase boundary moving past the inclusion.

The mechanics of the two-dimensional problem involve a balance between the energy that the phase boundary would require to deviate from the compatible direction imposed by the crystalline basis and the elastic energy that would be required for the large distortions were the phase boundary to move past the inclusion while remaining straight. The single variant of martensite is not compatible with the inclusion, and the acoustic wave provides enough energy for microstructure to begin nucleating that then grows and takes energy away from the original phase boundary.

There is experimental evidence of such a mechanism, in micrographs that show the long slivers that are remnants of untransformed material near inclusions (James, 2005).

We have repeated these calculations with smaller and larger driving force. With very small driving force, the acoustic wave passes through the inclusion with no nucleation. The original phase boundary gradually slows down and eventually comes to rest before reaching the inclusion. With a large driving force across the phase boundary, we find that the motion of the phase boundary is relatively unaffected by the presence of the inclusion in its movement across the domain, and it causes large deformations in the inclusion as it sweeps over it (Figure 2.13). Some acoustic waves are reflected back due to the presence of the inclusion, as can be seen in the figure.

The results above do not depend strongly on the orientation of the anisotropy in the inclusion. We have repeated the calculations with the anisotropy rotated by angles of $\frac{\pi}{4}$ and $\frac{\pi}{8}$, and we get similar results. The rotation of the anisotropy corresponds to the inclusion having different orientations of the crystalline lattice.

2.8 Discussion

In this paper, we have examined the kinetics of phase transformations in the peridynamic formulation of continuum mechanics. We find that phase boundaries nucleate and propagate naturally and uniquely in this theory. We only need to specify the interparticle interaction law and do not need to specify any additional conditions like the nucleation criterion or the kinetic relation. Further, we characterize the conditions under which nucleation occurs and the kinetic relations that govern the propagation of a phase boundary. Furthermore, we find that topology transitions occur easily and naturally. Finally, numerical simulations are easy to implement since they involve no spatial derivatives. For all these reasons, we conclude that peridynamics is a very attractive theory for computational studies of martensitic phase transformations.

It is common practice in the literature to study quasistatic hysteresis using a sequence of incremental loading followed by equilibration as we did in Section 2.3. Our results, in particular our analysis of nucleation, shows that this can depend very much on the numerical method and the size of the incremental load step. Therefore, one should be cautious in interpreting the results of such computations.

We have studied nucleation viewing it as a dynamic instability. It provides a criterion that is consistent with our numerical studies. Our viewpoint is different from the classical energetic view of nucleation. It also differs from the viewpoint of Abeyaratne and Knowles (1991b) based on thermodynamic driving force. In the latter two views, one examines whether a perturbation that introduces a second phase grows, while we examine the dynamic stability of a slightly perturbed single phase solution (it is not necessary for the perturbation to be large enough to include the other stable phase). Therefore, a relation between our viewpoint and the others is

unclear. As peridynamics is able to resolve the structure of the interface rather than treating it as a sharp discontinuity, we speculate that our analysis may be considered microscopic as opposed to the alternate viewpoints. This distinction places the usual regularized theories on the microscopic side, and hence this criterion may hold in those theories as well.

We have revisited the regularized continuum theory with strain gradients and viscosity and studied nucleation from the viewpoint of dynamic stability in Appendix 2.B. We have found an important difference between that theory and peridynamics. In the regularized continuum theory, the defect size depends only on the size of the region in the unstable phase and not on the difference between the ambient strain and the unstable strain. This reflects the local nature of this theory. In contrast, in peridynamics, which is a nonlocal theory, the defect size depends on both the size of the region in the unstable phase and on the difference between the ambient strain and the unstable strain. This has important consequences. Suppose we introduce a large perturbation in a small region of space. Whether this leads to a nucleation is independent of ambient strain in the regularized theory, but significantly dependent in the peridynamic theory. Consequently, if the spatial extent of this perturbation is small enough, it will not lead to nucleation in the regularized theory no matter how close the ambient strain is to the unstable phase, but will do so in the peridynamic formulation. We believe that this is the reason why nucleation has been found to be extremely difficult in computational studies of the regularized and phase-field theories and various researchers have had to resort to noise, pre-nuclei and low-barrier regions. In contrast, the calculations in this paper show that nucleation is relatively simple in this formulation.

Our calculations show that phase boundaries may be viewed as traveling waves. These traveling waves have leading and trailing oscillations that decay as we move away from the phase boundary. The rate of decay depends on viscosity, but the wavelength is relatively independent. The velocity of the traveling wave depends on the average far field conditions only through a driving force, so that this analysis leads to a kinetic relation. The kinetic relation with viscosity leads to large dissipation for

small speeds, but curiously smaller dissipation for larger phase boundary velocities, compared to the inviscid case. We do not understand this curious cross-over, but note that a similar result has been found in regularized theories (Abeyaratne and Knowles, 1991a). The kinetic relation goes continuously through the origin (i.e., the velocity and the driving force approach zero together). There is also a limiting velocity which is the sound speed of both phases (these are assumed equal and constant in the trilinear material). We have also carried out similar calculations for a material with a cubic polynomial stress response function. The kinetic relation with viscosity does not have a limiting velocity, and this is not surprising since the high strain phase has unbounded sound speed.

While small amplitude waves in either of the stable phases of our peridynamic material are dispersive, it is interesting that we find traveling wave structures that involve all phases. Like other solitons, we believe that the nonlinearity and the dispersion balance each other for special structures and allow them to be traveling waves.

We close by pointing out two interesting and open problems. We have shown that nucleation and kinetics arise from a specification of a force field in the peridynamic formulation. However, the range of nucleation conditions and kinetic relations that can be obtained from within the peridynamic formulation remains unknown. Similarly, it remains unclear whether one can alter the kinetic and static properties independently. Finally, an examination of nucleation from the point of view of dynamic instability in higher dimensions and also in atomistic systems would be very interesting.

2.A Bounds on the spectrum of a non-ideal defect

We derive here bounds on the spectrum of a non-ideal defect, using the results that we have for an ideal defect. We recall that a non-ideal defect has a non-trivial mixed region as described in Figure 2.7(b). For such a defect, with a given δ^u and δ^l, we expect that an ideal defect of size δ will be more stable than a non-ideal defect when

$\delta^l = \delta$, as the non-ideal defect would have as large an inner unstable region as the ideal defect, as well as more unstable springs outside this inner region, while the ideal defect would have no unstable springs outside the inner region. Similarly, we expect that an ideal defect of size δ will be less stable than a non-ideal defect when $\delta^u = \delta$, as the non-ideal defect would have some stable springs in the inner region while the ideal defect would have only unstable springs in the inner region. We make these bounds rigorous by means of standard inequalities that are well-known:

$$\int_\Omega f(x)g(x)\ dx \leq \left(\int_\Omega f(x)^2\ dx\right)^{\frac{1}{2}} \left(\int_\Omega g(x)^2\ dx\right)^{\frac{1}{2}} \tag{2.31a}$$

$$\int_\Omega |f(x)+g(x)|^2\ dx \leq \left(\left(\int_\Omega f(x)^2\ dx\right)^{\frac{1}{2}} + \left(\int_\Omega g(x)^2\ dx\right)^{\frac{1}{2}}\right)^2 \tag{2.31b}$$

$$\int_\Omega |f(x)|\ |g(x)|\ dx \leq |f(x)|_{\max} \int_\Omega |g(x)|\ dx \tag{2.31c}$$

for $f(x), g(x) \in L_2(\Omega)$.

For a non-ideal defect with radii δ^u and δ^l, where $\delta^u = \delta$, we write the inner product:

$$\begin{aligned}
I_{\delta^u}(v) &= \int_{\mathbb{R}^2-(-\delta,\delta)^2} e^{-(x'-x)^2}\left(v(x)^2 - v(x)v(x')\right)\ dx\ dx' \\
&\quad + \int_{(-\delta,\delta)^2} K(x,x')e^{-(x'-x)^2}\left(v(x)^2 - v(x)v(x')\right)\ dx\ dx' \\
&= \int_{\mathbb{R}^2} e^{-(x'-x)^2}\left(v(x)^2 - v(x)v(x')\right)\ dx\ dx' \\
&\quad -2\int_{(-\delta,\delta)^2} e^{-(x'-x)^2}\left(v(x)^2 - v(x)v(x')\right)\ dx\ dx' \\
&\quad + \int_{(-\delta,\delta)^2} (1+K(x,x'))\, e^{-(x'-x)^2}\left(v(x)^2 - v(x)v(x')\right)\ dx\ dx' \\
&= I_\delta(v) \\
&\quad + \int_{(-\delta,\delta)^2} (1+K(x,x'))\, e^{-(x'-x)^2}\left(v(x)^2 - v(x)v(x')\right)\ dx\ dx'
\end{aligned}$$

where $K(x,x')$ is an indicator function that is -1 when x, x' are connected by an

unstable spring, and +1 when they are connected by a stable spring. The second term in the final form above indicates the difference between the inner product of a non-ideal defect and that of an ideal defect.

We normalize $v(x)$ by setting $v(x)$ to have unit L_2 norm over a finite region larger than δ^u, while retaining the restriction that $v(x)$ is such that the integrals appearing in the inner product are bounded.

Since $K(x, x')$ is symmetric in its arguments, we can exchange x, x' in the second term and add the result to the original integral to arrive at:

$$\begin{aligned}
&\int_{(-\delta,\delta)^2} (1 + K(x, x'))\, e^{-(x'-x)^2} \left(v(x)^2 - v(x)v(x')\right)\ dx\ dx' \\
&\quad = \frac{1}{2} \int_{(-\delta,\delta)^2} (1 + K(x, x'))\, e^{-(x'-x)^2} \left(v(x) - v(x')\right)^2\ dx\ dx' \qquad (2.32)
\end{aligned}$$

where the integrand is non-negative everywhere on the domain of integration and hence this term is bounded below by 0. For an upper bound on this term:

$$\begin{aligned}
&\frac{1}{2} \int_{(-\delta,\delta)^2} (1 + K(x, x'))\, e^{-(x'-x)^2} \left(v(x) - v(x')\right)^2\ dx\ dx' \\
&\leq \int_{(-\delta,\delta)^2} \left(v(x) - v(x')\right)^2\ dx\ dx' \\
&\leq \int_{(-\delta,\delta)} \left(\left(\int_{(-\delta,\delta)} v(x)^2\ dx' \right)^{\frac{1}{2}} + \left(\int_{(-\delta,\delta)} v(x')^2\ dx' \right)^{\frac{1}{2}} \right)^2 dx \\
&\leq \int_{(-\delta,\delta)} \left(v(x)\, (2\delta^u)^{\frac{1}{2}} + 1 \right)^2\ dx \\
&\leq \int_{(-\delta,\delta)} v(x)^2\, (2\delta^u)\ dx + \int_{(-\delta,\delta)} 1\ dx + 2 \int_{(-\delta,\delta)} v(x)\, (2\delta^u)^{\frac{1}{2}}\ dx \\
&\leq 8\delta^u
\end{aligned}$$

where we have used inequality (2.31c) to go to the second step, inequality (2.31b) to go to the third step, the normalization of $v(x)$ to bound the second term and go the fourth step, expanded the square to reach the fifth step, used again the normalization of $v(x)$ to bound the first term and inequality (2.31a) to bound the third term as

follows:

$$\int_{(-\delta,\delta)} v(x)\,(2\delta^u)^{\frac{1}{2}}\ dx \leq \left(\int_{(-\delta,\delta)} v(x)^2\ dx\right)^{\frac{1}{2}} \left(\int_{(-\delta,\delta)} (2\delta^u)\ dx\right)^{\frac{1}{2}}$$

and using again the normalization of $v(x)$.

We also see that the integrand in the above expression is 0 in the interior of the square $(-\delta^l, \delta^l)^2$ and hence has no contribution, and the integral in this region can be bounded above by $8\delta^l$ in the same manner as for the integral over the square $(-\delta, \delta)^2$. So, we can now write the upper and lower bounds as:

$$0 \leq \frac{1}{2}\int_{(-\delta,\delta)^2} (1 + K(x,x'))\, e^{-(x'-x)^2}\,(v(x) - v(x'))^2\ dx\ dx' \leq 8\left(\delta^u - \delta^l\right)$$

We now turn to the case when the non-ideal defect has $\delta^l = \delta$. Writing the inner product:

$$\begin{aligned}
&I_{\delta^l}(v) \\
&= \int_{\mathbb{R}^2-(-\delta^u,\delta^u)^2} e^{-(x'-x)^2}\left(v(x)^2 - v(x)v(x')\right)\ dx\ dx' \\
&\quad - \int_{(-\delta,\delta)^2} e^{-(x'-x)^2}\left(v(x)^2 - v(x)v(x')\right)\ dx\ dx' \\
&\quad + \int_{(-\delta^u,\delta^u)^2-(-\delta,\delta)^2} K(x,x')e^{-(x'-x)^2}\left(v(x)^2 - v(x)v(x')\right)\ dx\ dx' \\
&= \int_{\mathbb{R}^2} e^{-(x'-x)^2}\left(v(x)^2 - v(x)v(x')\right)\ dx\ dx' \\
&\quad -2\int_{(-\delta,\delta)^2} e^{-(x'-x)^2}\left(v(x)^2 - v(x)v(x')\right)\ dx\ dx' \\
&\quad - \int_{(-\delta^u,\delta^u)^2-(-\delta,\delta)^2} (1 - K(x,x'))\, e^{-(x'-x)^2}\left(v(x)^2 - v(x)v(x')\right)\ dx\ dx' \\
&= I_\delta(v) \\
&\quad - \int_{(-\delta^u,\delta^u)^2-(-\delta,\delta)^2} (1 - K(x,x'))\, e^{-(x'-x)^2}\left(v(x)^2 - v(x)v(x')\right)\ dx\ dx'
\end{aligned}$$

We can bound the difference between inner products following the same steps as for the previous bound with the appropriate modifications to arrive at the analogous bounds.

We summarize the results of these bounds:

$$I_\delta(v) \leq I_{\delta^u}(v) \leq I_\delta(v) + 8\left(\delta^u - \delta^l\right) \quad \text{when } \delta^u = \delta \tag{2.33a}$$

$$I_\delta(v) - 8\left(\delta^u - \delta^l\right) \leq I_{\delta^l}(v) \leq I_\delta(v) \quad \text{when } \delta^l = \delta \tag{2.33b}$$

for a given $v(x)$. We can immediately see from these bounds that if $\text{erf}(\delta^u) < \frac{1}{2}$, the non-ideal defect must be stable, and if $\text{erf}(\delta^l) > \frac{1}{2}$, the non-ideal defect must be unstable.

2.B Nucleation in a regularized theory

We study nucleation in a classical continuum theory augmented with viscosity and strain gradient (Abeyaratne and Knowles, 1991a). We use their model here without the viscous dissipation:

$$\rho\partial_{tt}u(x,t) = \partial_x(\hat{\sigma}(\partial_x u(x,t))) - \rho\lambda\partial_{xxxx}u(x,t) \tag{2.34}$$

where λ is the coefficient of surface energy and $\hat{\sigma}(\cdot)$ is the non-monotone stress response function.

Following the procedure that we used to study the peridynamic theory, we assume that a low strain field evolves and leads to a region of unstable strain. We then linearize the equations around this state and test the stability as a function of the defect size. For simplicity, we use a stress-response function that is bilinear and with equal and opposite slopes $\pm E_0 (E_0 > 0)$ on the branches. Adding a small perturbation $\epsilon v(x,t)$ to the displacement field $u(x,t)$ and differentiating the resulting equation with respect to ϵ leads to the linearized equation in $v(x,t)$:

$$\rho\partial_{tt}v(x,t) = \partial_x(E(x)\partial_x v(x,t)) - \rho\lambda\partial_{xxxx}v(x,t) \tag{2.35}$$

where $E(x) = \hat{\sigma}'(u(x,t)) = \pm E_0$ is the slope of the stress response and switches between stable and unstable as a function of position, $E(x) = -E_0$ for $|x| < \delta$ and $E(x) = E_0$ elsewhere.

Decomposing $v(x,t) = v(x)e^{i\omega t}$ into sinusoidal modes and taking the inner product $I_\delta^{\text{sg}} = \langle v(x), L_\delta^{\text{sg}} v(x) \rangle$ gives

$$I_\delta^{\text{sg}}(v) = \int_{\mathbb{R}} \rho\lambda v(x) v^{(4)}(x)\ dx - \int_{\mathbb{R}} E_0 v(x) v^{(2)}(x)\ dx + \int_{(-\delta,\delta)} 2E_0 v(x) v^{(2)}(x)\ dx$$

where the inner product is defined as in peridynamics.

Taking the limit of $\delta = 0$ and using the decomposition $v_k(x) = e^{ikx}$ allows us to calculate the spectrum $\rho\lambda k^4 + E_0 k^2$ which is stable for $k > 0$.

Taking the limit of $\delta \to \infty$ and using the decomposition $v_k(x) = e^{ikx}$, we find the spectrum is $\rho\lambda k^4 - E_0 k^2$, which is unstable for $k < \frac{1}{\gamma}$ where $\gamma := \sqrt{\rho\lambda/E_0}$ is the lengthscale associated with the strain gradient model. The strain gradient theory differs from the peridynamic theory in that the surface energy contribution has a stabilizing effect in both the stable and unstable regions, whereas in peridynamics the entire energy changes sign in the unstable regions.

It is straightforward to show that the operator is unstable at finite δ by using a test function that is localized within the defect. To show that the operator is stable for finite δ, we use integration by parts to rewrite the surface energy contribution, and rescale $v(x) = \tilde{v}(x/\delta) = \tilde{v}(y)$. This gives

$$I_\delta^{\text{sg}}(v) = \frac{1}{\delta^2 E}\left(\left(\frac{\gamma}{\delta}\right)^2 \int_{\mathbb{R}} \left(\tilde{v}^{(2)}(y)\right)^2\ dy - \int_{\mathbb{R}} \tilde{v}(y)\tilde{v}^{(2)}(y)\ dy + \int_{(-1,1)} 2\tilde{v}(y)\tilde{v}^{(2)}(y)\ dy\right)$$

From the continuity and jump requirements on $v(x,t)$ and its derivatives (Abeyaratne and Knowles, 1991a), the first integral in the expression above is positive and finite, and the remaining integrals are finite. So, for any $\tilde{v}(y)$, we can always find a value of $\delta > 0$ that makes the first positive integral sufficiently large that the entire expression is positive. The form of the expression above also shows that the critical defect size

scales with the internal length scale of the material γ prescribed by the choice of surface energy coefficient.

This calculation highlights an important difference between the non-local peridynamic theory and strain gradient theories. In the peridynamic theory, the formation of a small area of unstable phase that is surrounded by a stable region of low strain phase that is close to the peak strain has a large effective defect size due to the fact that many of the surrounding springs are easily stretched beyond the peak strain. Similarly, a defect surrounded by low strain phase that is well below the peak strain has a smaller effective size. This dependence of the effective defect size on the strain in the neighborhood is unique to peridynamics. The ability of peridynamics to capture the effect of the surroundings makes it very different from a strain gradient theory in this respect.

Bibliography

Abeyaratne, R., Knowles, J. K., 1990. On the driving traction on a surface of a strain discontinuity in a continuum. J. Mech. Phys. Solids 38, 345–360.

Abeyaratne, R., Knowles, J. K., 1991a. Implications of viscosity and strain gradient effects for the kinetics of propagating phase boundaries in solids. SIAM J. Appl. Math. 51 (5), 1205–1221.

Abeyaratne, R., Knowles, J. K., 1991b. Kinetic relations and the propagation of phase boundaries in solids. Arch. Rational Mech. Anal. 114, 119–154.

Anderson, E., Bai, Z., Bischof, C., Blackford, S. L., Demmel, J. W., Dongarra, J. J., DuCroz, J., Greenbaum, A., Hammarling, S., McKenney, A., Sorensen, D., 1999. LAPACK User's Guide, 3rd Edition. Society for Industrial and Applied Mathematics.

Artemev, A., Jin, Y., Khachaturyan, A., 2001. Three-dimensional phase field model of proper martensitic transformation. Acta Mater. 49 (7), 1165–1177.

Ball, J. M., James, R. D., 2005. Metastability in martensitic phase transformations, in preparation.

Bhattacharya, K., 2003. Microstructure of martensite. Oxford University Press.

Christian, J. W., 1975. The theory of transformations in metals and alloys. Pergamon.

Dondl, P. W., Zimmer, J., 2004. Modeling and simulation of martensitic phase transitions with a triple point. J. Mech. Phys. Solids 52 (9), 2057–2077.

Engl, H. W., Hanke, M., Neubauer, A., 2000. Regularization of inverse problems. Kluwer Academic Publishers.

Eshelby, J. D., 1956. Solid State Physics. Vol. 3. Academic Press, pp. 17–144.

Eshelby, J. D., 1975. The elastic energy-momentum tensor. J. Elasticity 5, 321–335.

James, R. D., 2005. Unpublished micrographs.

Killough, M. G., 1998. A diffuse interface approach to the development of microstructure in martensite. Ph.D. thesis, New York University.

Kloucek, P., Luskin, M., 1994. Computational modeling of the martensitic transformation with surface energy. Math. Comput. Model. 20, 101–121.

Kunin, I. A., 1982. Elastic media with microstructure. Vol. 26 of Springer Series in Solid-State Sciences. Springer-Verlag.

Lefloch, P., 1993. Propagating phase boundaries: formulation of the problem and existence via the Glimm method. Arch. Rational Mech. Anal. 123, 153–197.

Lei, Y., Friswell, M. I., Adhikari, S., 2006. A Galerkin method for distributed systems with non-local damping. Int. J. Solids Struct. 43, 3381–3400.

Olson, G. B., Roitburd, A. L., 1992. Martensite. ASM, Ch. Martensitic Nucleation, pp. 149–174.

Porter, D., Stirling, D. G. S., 1990. Integral equations. Cambridge University Press.

Purohit, P. K., 2001. Dynamics of phase transitions in strings, beams and atomic chains. Ph.D. thesis, California Institute of Technology.

Silling, S. A., 2000. Reformulation of elasticity theory for discontinuities and long-range forces. J. Mech. Phys. Solids 48, 175–209.

Silling, S. A., Kahan, S., April 2004. Peridynamic modeling of structural damage and failure. In: Conference on High Speed Computing, Gleneden Beach, Oregon, USA.

Silling, S. A., Zimmermann, M., Abeyaratne, R., 2003. Deformation of a peridynamic bar. J. Elasticity 73, 173–190.

Truskinovsky, L., 1993. Kinks versus shocks. In: Fosdick, R., Dunn, E., Slemrod, M. (Eds.), Shock induced transitions and phase structures in general media. No. 52 in IMA. Springer -Verlag.

Truskinovsky, L., Vainchtein, A., 2005. Kinetics of martensitic phase transitions: Lattice model. SIAM J. Appl. Math. 66 (2), 533–553.

Wang, Y. Z., Chen, L. Q., Khachaturyan, A. G., 1994. Solid-solid phase transformations. The Min. Metals. Mater. Soc., Ch. Computer simulation of microstructure evolution in coherent solids, pp. 245–265.

Weckner, O., Abeyaratne, R., 2005. The effect of long-range forces on the dynamics of a bar. J. Mech. Phys. Solids 53, 705–728.

Zimmermann, M., 2002. Phase transformations in the one dimensional peridynamic theory, unpublished private communication.

Chapter 3

A real-space non-local phase-field model of ferroelectric domain patterns in complex geometries

---

Abstract

Ferroelectric perovskites are used in various MEMS devices due to the strong coupling between electric field and strain. They also have large nonlinear responses to optical excitation for which they have been proposed as elements of photonics devices. In these applications, ferroelectrics are machined to have complex geometries with complex arrangements of electrodes. It is therefore important to understand the domain patterns that form in these complicated geometries. However, available models assume unrealistic boundary conditions to be useful in these contexts.

We develop a real-space, non-local phase-field model to address this issue. The model is constructed for barium titanate, a tetragonal perovskite, by identifying the total energy consisting of Landau, domain wall and electrostatic contributions. The key issue is to resolve the electrostatic fields within the ferroelectric, as well as the stray or induced fields in the surroundings in a computationally efficient manner. We do so by using a boundary element method to account for the non-local electrostatic contributions, and this makes the modeling of free surfaces computationally tractable.

We use the method to study the behavior of a ferroelectric crystal with patterned electrodes, a geometry that is of interest in the design of electronic and photonic

devices with ferroelectrics. The mechanical and electrical effects of a notch in such a device are also examined as a first step towards a consistent study of the role of microstructure formation in the fracture process of ferroelectric materials.

3.1 Introduction

Ferroelectric materials are currently used for actuation and in high-speed memories. They have also been proposed as elements of microwave circuits and as photonic switches at small lengthscales. Modern devices are shrinking to the scale of the domain microstructures, and proposed designs exploit microstructure evolution as device elements (Bhattacharya and James, 2005; Dayal and Bhattacharya, 2006b). Further, fracture processes in ferroelectrics are strongly coupled to microstructure evolution. Design and manufacture of new devices and predicting failure requires an understanding of the detailed microstructure in realistic geometries.

Understanding domain patterns in ferroelectrics and their evolution in response to applied loads has motivated much recent research. The time-dependent Devonshire-Landau-Ginzburg (TDGL) framework has been applied using phase-field techniques and has led to important insights into the overall behavior, examples being the formation of microstructure in barium titanate (Hu and Chen, 1998), lead titanate (Li et al., 2002) and the mechanics of domain switching (Wang et al., 2004). The ability of TDGL phase-field methods to model these microstructural phenomena makes them good candidates for further efforts in this direction.

However, electrostatic fields generated by devices are *nonlocal*. Stray fields extend not only within the material but over all of space. Current numerical methods to evaluate electrostatic contributions to the free energy rely on the FFT technique for efficient computation. This restricts analysis to periodic domains. Other approaches focus on completely shielded systems that are completely covered by electrodes and hence do not allow stray fields outside the body. As devices of interest grow smaller and are micromachined to have complex features, there is a need to extend the framework to deal with the complex geometries that can not be adequately understood with

current techniques.

We present here our implementation of a *boundary element* technique that allows for the accurate and efficient resolution of electrostatic fields over all space, without the assumptions of periodicity or shielding, and allows us to deal with complex geometries. Boundary element techniques have been developed and are standard techniques in the context of electromagnetism, acoustics and other areas that require the resolution of fields over finite regions but with the boundary conditions specified over an infinite domain. Examples of implementations of boundary element techniques can be found in (Wrobel, 2002), (Kane, 1994) and references contained there.

We couple our boundary element implementation to a recently-developed phase-field model (Zhang and Bhattacharya, 2005) for the evolution of domain patterns in ferroelectrics, and present examples of computations and geometries that are possible with this technique. This phase field model has been used to characterize domain patterns that are formed in barium titanate under different electromechanical loadings and captures the essential features. In this model, the electric field is formulated explicitly in real-space rather than in a periodic geometry, as is typical in previous work involving phase-field models. We exploit the real-space formulation to implement the boundary element technique.

The magnetostatic equation that arises in the study of microstructure in ferromagnetics, i.e., micromagnetism, is similar in form to the electrostatics equation and can be coupled to a phase field model of the sort we describe in this paper, or to other micromechanical models. An important difference is that there are no free charges in ferromagnetism; in contrast, charged defects exist in ferroelectrics though we neglect their consideration here. Another difference is that the magnitude of the magnetization is a constant in ferromagnets and only orientational change is allowed by paying an energy penalty; in contrast, the analogous polarization can change both magnitude and orientation by paying an energy penalty. While these differences lead to important contrasts in the behavior of ferroelectrics and ferromagnets, the implementation of the boundary element method in micromagnetism is an area of active research (see Fidler and Schrefl, 2000, and references there).

We begin by presenting the phase-field equations and the associated gradient flow evolution equations in Section 3.2. In Section 3.3, we present the techniques we use to solve the evolution equations, emphasizing the details of the boundary element technique. We present examples to test the technique in Sections 3.4, 3.5, and 3.6. We conclude with a discussion of our results in Section 3.7.

3.2 The phase-field formulation

From Shu and Bhattacharya (2001), we have that the potential energy E of a ferroelectric body Ω can be written:

$$E(\boldsymbol{\varepsilon}, \mathbf{p}) = \int_{\Omega} \left[U(\nabla \mathbf{p}) + W(\boldsymbol{\varepsilon}, \mathbf{p}) \right] d\Omega + \frac{\epsilon_0}{2} \int_{\mathbb{R}^3} |\nabla \phi|^2 dV \tag{3.1}$$

and is a function of the elastic strain field $\boldsymbol{\varepsilon}$ and the polarization field $\mathbf{p}$. The contributions to the energy come from a surface energy U that penalizes gradients in $\mathbf{p}$ and models the energy contributions from domain walls, an anisotropy energy W that penalizes $\mathbf{p}$ not being aligned with the local crystallographic basis, and the final term represents the electrostatic energy contained in the electric fields $\mathbf{E} = -\nabla\phi$, where ϕ is obtained by solving Maxwells equation:

$$\nabla \cdot (\mathbf{p} - \epsilon_0 \nabla \phi) = 0 \quad \text{over} \quad \mathbb{R}^3 \tag{3.2}$$

The first 2 terms in the energy are local to the body being considered, while the electrostatic contribution requires evaluation over all space.

Following Zhang and Bhattacharya (2005), we model the evolution of the system through gradient flow of the potential energy. The evolution equations are obtained by taking the first variation:

$$\mu \frac{dp_i}{dt} = \left(\frac{\partial U}{\partial p_{i,j}} \right)_{,j} - \frac{\partial W}{\partial p_i} - \phi_{,i} \quad \text{over} \quad \Omega \tag{3.3a}$$

$$\left(\frac{\partial W}{\partial \varepsilon_{ij}}\right)_{,j} = 0 \quad \text{over} \quad \Omega \tag{3.3b}$$

$$p_{i,i} - \epsilon_0 \phi_{,ii} = 0 \quad \text{over} \quad \mathbb{R}^3 \tag{3.3c}$$

The boundary conditions for the gradient flow equations arise from the variational procedure. We require that $\nabla \mathbf{p} \cdot \mathbf{n} = 0$ associated with the evolution of $\mathbf{p}$, conventional elasticity boundary conditions for the elastic equilibrium equation, and voltage specified at certain points (i.e., on the electrodes) and field decaying at infinity associated with the electrostatic field.

In this paper, we work with barium titanate, and specialize the constitutive models for U and W for this material. Further, we restrict ourselves to a two-dimensional plane strain system for the computational implementation, but our formulation is general and can be easily extended to a fully three-dimensional calculation.

We use the same material model that was tested in Zhang and Bhattacharya (2005) and found to be satisfactory for understanding the evolution of domain structures in barium titanate. We use a simple form for the surface energy that regularizes the system and prevents the formation of sharp domain walls:

$$U(\nabla \mathbf{p}) = \frac{a_0}{2}\left(p_{1,1}^2 + p_{1,2}^2 + p_{2,1}^2 + p_{2,2}^2\right) \tag{3.4}$$

We model the anisotropy energy using a Landau polynomial approach:

$$\begin{aligned} W(\boldsymbol{\varepsilon}, \mathbf{p}) = \frac{a_1}{2}\left(p_1^2 + p_2^2\right) \quad &+ \quad \frac{a_2}{4}\left(p_1^4 + p_2^4\right) + \frac{a_3}{2} p_1^2 p_2^2 + \frac{a_4}{6}\left(p_1^6 + p_2^6\right) + \frac{a_5}{4} p_1^4 p_2^4 \\ &+ \quad (\boldsymbol{\varepsilon} - \boldsymbol{\varepsilon}_T(\mathbf{p})) \cdot \mathbb{C} \cdot (\boldsymbol{\varepsilon} - \boldsymbol{\varepsilon}_T(\mathbf{p})) \end{aligned} \tag{3.5}$$

where we have assumed that the energy due to misfit strain is quadratic, i.e., linear elasticity, and the stress-free strain is coupled to the local polarization.

We use the material constants $a_0, a_1, a_2, a_3, a_4, a_5, \mathbb{C}$ and the expression for $\boldsymbol{\varepsilon}_T(\mathbf{p})$ chosen by Zhang and Bhattacharya (2005), as these have been shown to adequately

reproduce the response of barium titanate.

3.3 Solving the phase-field evolution equations

Having specified the governing equations and chosen an appropriate material model, we now have sufficient equations to solve boundary value problems. In this section, we detail the numerical method that we will use. For simplicity, we have used a square finite-difference grid, and confine ourselves to two dimensions. Further, we have assumed that the strains are small, and hence there is no difference between current and reference configurations when solving the electrostatic equations.

Our strategy is to begin with an initial guess for the strain and polarization fields in the interior of the ferroelectric, and evolve in the direction of the gradient flow until we reach an equilibrium state. At each time step of the gradient flow, as we update the polarization, we solve the electrostatic and elastostatic equations to find the strain and electric potential caused by the updated polarization field. These new fields are then used to again update the polarization, and the process is repeated until we are sufficiently close to equilibrium.

The polarization update is achieved using a simple explicit time marching scheme, with conventional finite differences to model spatial derivatives. Similarly, the elasticity equations are solved by writing the equations in terms of the displacement and then discretizing the displacement equations in space with the appropriate boundary conditions.

As we have seen in the previous section, the electrostatic potential is obtained from the solution of Maxwell's equation over all space. However, we have from the equation for the polarization update that we only require the potential field at every point in the body. This leads to the boundary element technique as a means of transforming the nonlocal problem of obtaining the electrostatic potential by solving over all space, to a local problem that provides the solution only over the body of interest. This transformation provides us with a means of efficiently solving the electrostatic equations. However, at the same time, we need to ensure that the

boundary conditions are accurately satisfied.

The key idea behind the boundary element method is the Dirichlet to Neumann map, i.e., we transform our boundary conditions from being partially specified on the boundary (through a given voltage at the electrodes) and partially specified at infinity (through the requirement that the field decays far away) to simpler boundary conditions: that the surface charge is specified *everywhere* on the boundary, *including* at the electrodes.

We are given the charge density in the interior due to the imbalance of the polarization pointwise, and further, we are given the surface charge density by the change in polarization at the exposed surfaces. However, we are not given the charge at regions covered by electrodes; instead, we are given the voltages there. We begin by replacing the electrodes by surface charge distributions; however, these surface charge distributions are unknown. They are not arbitrary, however, as they are required to satisfy that the potential due to the charges (combined from the known and unknown) matches that specified at the electrodes. This matching condition provides us with the ability to solve for the unknown surface charge distributions.

Once we have solved for them, the charge distribution everywhere in the body is known to us. We can then superpose the potential due to each of these charges to obtain the potential at any point we desire. We use this ability to find the potential over the entire boundary, leaving us with the simple task of obtaining the potential in the interior of a domain with potential specified on the entire boundary. We can see that we have gone from a mixture of charge and potential boundary conditions (Dirichlet and Neumann) to a purely boundary potential problem (Dirichlet).

We now provide some details on the electrostatics solution technique. In what follows, we note that we are solving the electrostatics problem at a given instant in time, and hence, the polarization is treated as a fixed quantity that is specified for the purposes of solving for the electric field.

Writing out the electrostatics equation and its boundary conditions:

$$\epsilon_0 \nabla \cdot \nabla \phi(\mathbf{x}) = \nabla \cdot \mathbf{p}(\mathbf{x}) =: \rho(\mathbf{x}) \quad \text{over} \quad \mathbb{R}^3 \tag{3.6a}$$

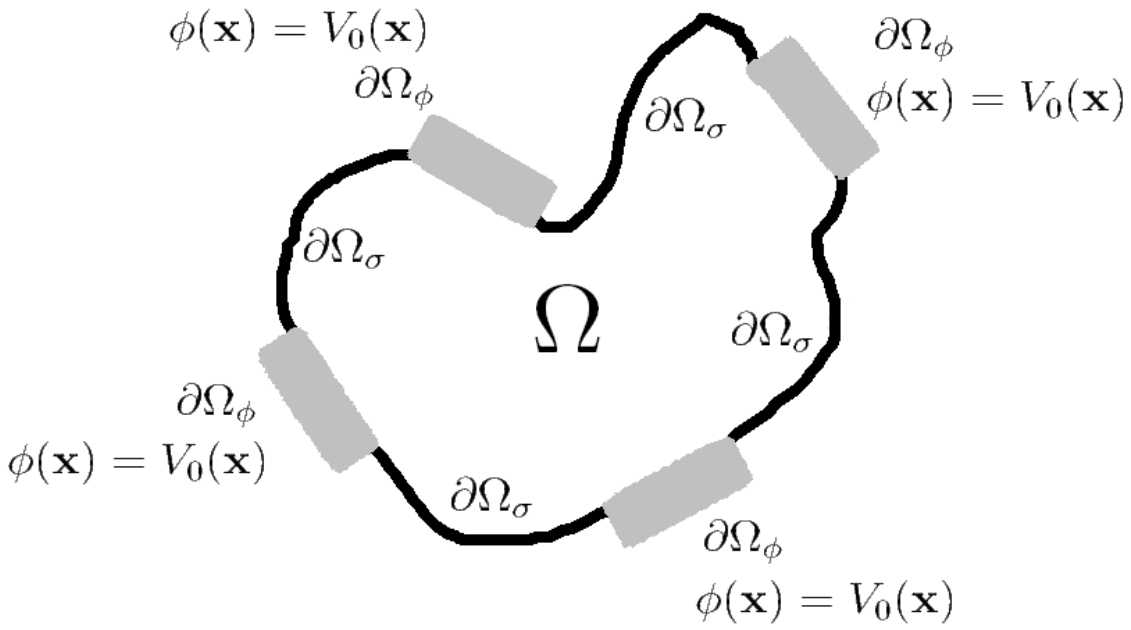

Figure 3.1: Boundary conditions for the electrostatics problem.

$$\phi(\mathbf{x}) = V_0(\mathbf{x}) \quad \text{on} \quad \partial\Omega_\phi \tag{3.6b}$$

$$\epsilon_0[\![\nabla\phi(\mathbf{x})]\!] \cdot \hat{\mathbf{n}} = \mathbf{p}(\mathbf{x}) \cdot \hat{\mathbf{n}} =: \sigma(\mathbf{x}) \quad \text{on} \quad \partial\Omega_\sigma \tag{3.6c}$$

$$\nabla\phi(\mathbf{x}) \to 0 \quad \text{as} \quad (\mathbf{x}) \to \infty \tag{3.6d}$$

The notation: $\partial\Omega_\phi, \partial\Omega_\sigma$ are the portions of the boundary with electrodes, free surfaces respectively. As can be seen above, electrode boundaries have potential (voltage) specified and free surfaces have surface charge density (from discontinuous polarization) specified (Figure 3.1). We do not consider any other electrical boundary conditions in this work, and hence $\partial\Omega_\phi \cup \partial\Omega_\sigma = \partial\Omega$ covers the entire ferroelectric Ω. [1]

We begin by replacing the voltage boundary conditions over $\partial\Omega_\phi$ by surface charge

[1] The surface charge balance is not a boundary condition for the electrostatic equation, but comes from the weak form of the electrostatics equation at a discontinuity that is in this case the body surface. In our case, this discontinuity coincides with the boundary of the region of interest. This may not always be the case, as, for example, in a model of a PFM probe.

boundary conditions. These surface charges σ^* are unknown:

$$\epsilon_0 \nabla \cdot \nabla\phi(\mathbf{x}) = \rho(\mathbf{x}) \quad \text{over} \quad \mathbb{R}^3 \tag{3.7a}$$

$$\epsilon_0 [\![\nabla\phi(\mathbf{x})]\!] \cdot \hat{\mathbf{n}} = \begin{cases} \sigma(\mathbf{x}) & \text{on} \quad \partial\Omega_\sigma \\ \sigma^*(\mathbf{x}) & \text{on} \quad \partial\Omega_\phi \end{cases} \tag{3.7b}$$

$$\nabla\phi(\mathbf{x}) \to 0 \quad \text{as} \quad (\mathbf{x}) \to \infty \tag{3.7c}$$

Let $G(\mathbf{x}, \mathbf{x}')$ be the fundamental (Greens) solution to this equation that satisfies $G(\mathbf{x}, \mathbf{x}') \to 0 \quad \text{as} \quad |\mathbf{x} - \mathbf{x}'| \to \infty$. We can then write the solution for the potential as

$$\phi(\mathbf{x}) = \int_\Omega G(\mathbf{x}, \mathbf{x}')\rho(\mathbf{x}')d\mathbf{x}' + \int_{\partial\Omega_\sigma} G(\mathbf{x}, \mathbf{x}')\sigma(\mathbf{x}')d\mathbf{x}' + \int_{\partial\Omega_\phi} G(\mathbf{x}, \mathbf{x}')\sigma^*(\mathbf{x}')d\mathbf{x}' \tag{3.8}$$

Applying this relation to the boundary region $\partial\Omega_\phi$ where we know that $\phi(\mathbf{x}) = V_0(\mathbf{x})$:

$$V_0(\mathbf{x}) = \int_\Omega G(\mathbf{x}, \mathbf{x}')\rho(\mathbf{x}')d\mathbf{x}' + \int_{\partial\Omega_\sigma} G(\mathbf{x}, \mathbf{x}')\sigma(\mathbf{x}')d\mathbf{x}' + \int_{\partial\Omega_\phi} G(\mathbf{x}, \mathbf{x}')\sigma^*(\mathbf{x}')d\mathbf{x}' \tag{3.9}$$

This equation can now be solved for the unknown function $\sigma^*(\mathbf{x}')$. We do this on the finite difference grid by assuming that $\sigma^*(\mathbf{x}')$ is piecewise-constant, i.e., it has a specific constant value over the region associated with the corresponding grid point. Applying the equation above at each grid point in $\partial\Omega_\phi$ gives us a system of linear equations that are to be solved for the σ^*_m at each grid point:

$$\begin{aligned} V_{0_l} = \sum_{\{m:\mathbf{x}_m \in \Omega\}} G(\mathbf{x}_l, \mathbf{x}_m)\rho_m \Delta x^2 \quad &+ \sum_{\{m:\mathbf{x}_m \in \partial\Omega_\sigma\}} G(\mathbf{x}_l, \mathbf{x}_m)\sigma_m \Delta x \\ &+ \sum_{\{m:\mathbf{x}_m \in \partial\Omega_\phi\}} G(\mathbf{x}_l, \mathbf{x}_m)\sigma^*_m \Delta x \end{aligned} \tag{3.10}$$

This system of linear equations can be solved to find the unknown σ^*_m.

Now, we have available to us the surface charge density on the entire boundary as well as the charge density in the interior. This enables us to find ϕ at any point in space by using the fundamental solution (3.8), and in particular, we evaluate ϕ over the entire boundary $\partial\Omega$, and we denote this $\phi^*(\mathbf{x})$. The problem has now been reduced to finding the potential within a finite domain, given the charge density in the interior and the potential on the entire boundary. We have thus decoupled the electrical field problem in the interior from the exterior:

$$\epsilon_0 \nabla \cdot \nabla \phi(\mathbf{x}) = \rho(\mathbf{x}) \quad \text{in} \quad \Omega \tag{3.11a}$$

$$\phi(\mathbf{x}) = \phi^*(\mathbf{x}) \quad \text{on} \quad \partial\Omega \tag{3.11b}$$

and this can be solved using conventional and efficient techniques.

3.4 Closure domain microstructure at a free surface

The electrostatic equation and its associated boundary conditions (3.6) show that free surfaces can have associated with them concentrated electrostatic surface charges on the order of the polarization. The large electrostatic fields associated with the concentrated charge at free surfaces lead to significant contributions to the electrostatic portion of the potential energy. An attempt to reduce this electrostatic energy leads to the formation of microstructure in the vicinity of the free surface. However, this microstructure leads to an increase in the interfacial energy U, and possibly also stresses and an increase in the elastic energy. Thus, there is a complex competition between the electrostatic energy, the interfacial energy and elastic energy.

The general problem we are describing is in some ways similar to the problem of closure domains that has been examined in ferromagnetism[2]. This area is relatively

[2]We recall that as mentioned in Section 3.1, ferromagnetism differs from ferroelectricity in two important respects. Firstly, there are no free charges in ferromagnetism. Secondly, the magnitude of

much better studied in the context of ferromagnets compared to ferroelectrics. There exists a large literature considering theoretical aspects and coupled with considerable experimental efforts (see Hubert and Schafer, 1998, and references there). There has also been theoretical work on classifying the various closure domain structures expected in different limits of geometric aspect ratio as well as energetic contributions (reviewed in DeSimone et al., 2005). Such a comprehensive classification is as yet unavailable for ferroelectrics. The application of the boundary element technique may aid theoretical efforts by providing numerical clues to this problem.

In this section, we use the boundary element technique to numerically study a simple example of these closure domains. In particular, for a simple geometry and orientation of the free surface with respect to the crystal basis, we examine the effect of mechanical boundary conditions on the electric field that is generated outside the body.

We use a rectangular computational domain, and we use as starting point for the polarization field a domain pattern that consists of alternate vertical bands of upward (c^+) and downward (c^-) pointing domains. We use a grounded electrode on the bottom surface to approximate an infinite body, in the electrical sense. We also use periodicity in the horizontal direction. However, we assume that top surface has no electrodes. This leads to the formation of alternate regions of positive (negative) surface charges associated with the c^+ (c^-) polarizations ending on the free surface. To prevent long-range effects that would require us to model the entire body, we use equal volume fractions of the c^+ and c^- domains to achieve local charge balance. Further, the crystallographic basis is oriented along the rectangular directions for simplicity.

We have examined the closure patterns for two different sets of mechanical boundary conditions.

1. **Mechanically constrained:** This is an approximation to the closure microstructure on the surface of a large ferroelectric body. Boundary conditions

the magnetization (analogous to the polarization) is fixed. These differences could potentially lead to very different closure domain microstructures.

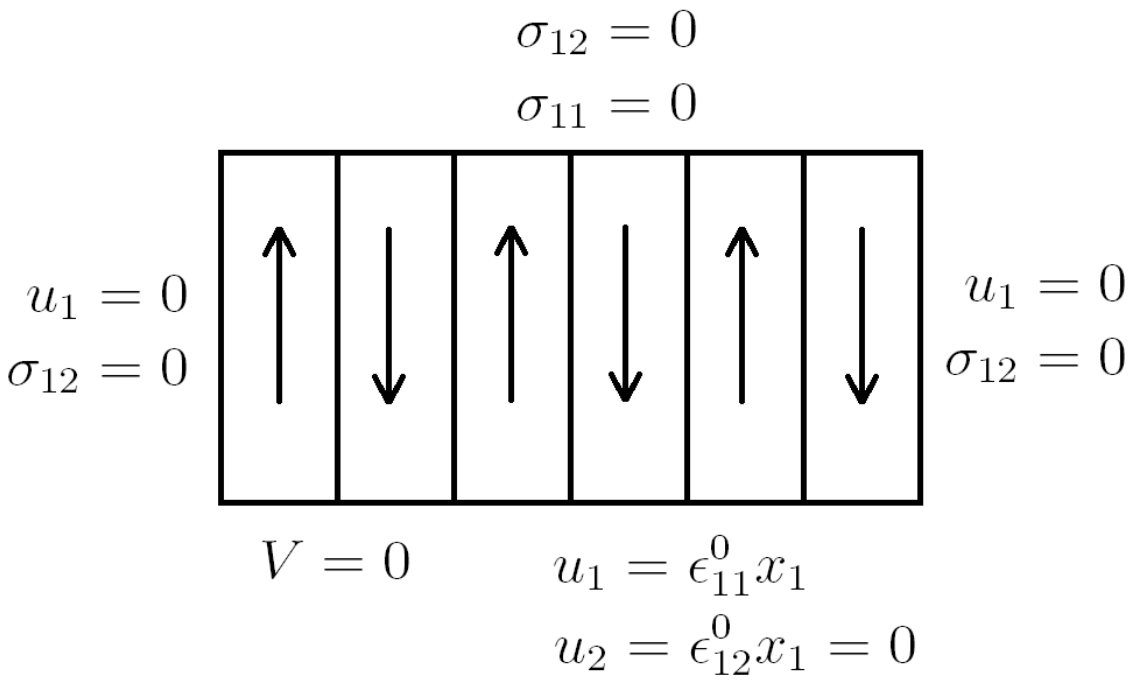

Figure 3.2: Boundary conditions and initial polarization field

consist of clamping the bottom face of the computational domain with zero vertical displacement and horizontal displacement to satisfy the stress-free strain value, and clamping the vertical faces in the horizontal direction at the value of the stress-free strain while keeping them shear traction free, and finally completely traction free on the vertical face (Figure 3.2).

2. **Mechanically unconstrained:** This is an approximation to the closure microstructure in a thin film, with the thickness of the computational domain on the order of the closure domains. We use an entirely traction-free boundary.

As mentioned above, this starting guess for the polarization has large electrostatic energy, and the polarization is evolved with a gradient flow scheme to minimize the total energy. This leads to the formation of closure domains as in Figure 3.3, where we have shown the second component of the polarization vector field. Except at the domain walls, the magnitude of the polarization is approximately constant (and has been normalized to 1). The polarization field for both sets of boundary conditions is similar.

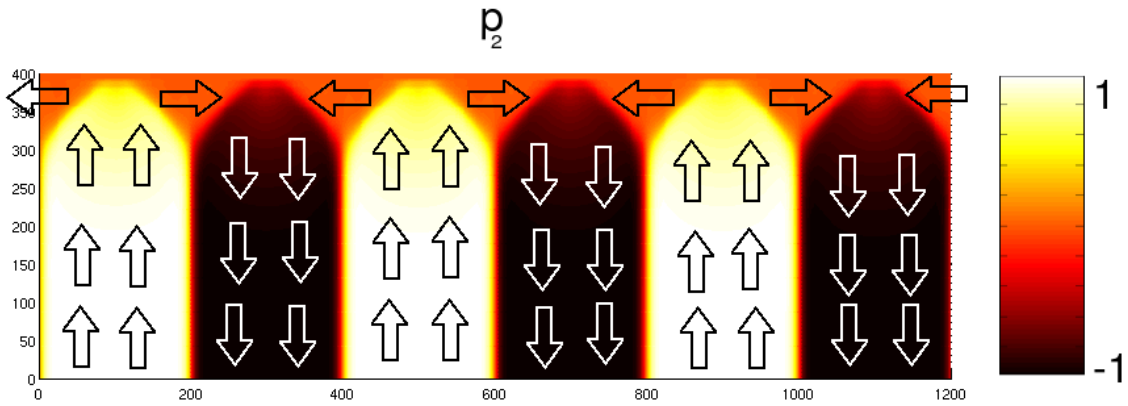

Figure 3.3: Equilibrium closure domain structure (p_2 field). The arrows are only to guide the reader.

However, the electrostatic potential that is built up outside the body is quite different in the two cases considered. From Figure 3.4, we see that the potential outside the body in the constrained case is considerably higher than in the thin film. This may be of relevance to current efforts to use such domain patterns for self assembly (Kalinin et al., 2002).

The closure domains that form are similar to those seen in tetragonal ferromagnetic materials and can be understood in terms of the same balance of energies (see Hubert and Schafer, 1998, and references there for details on the ferromagnetic case). The triangular closure domains that form allow for a large reduction in electrostatic energy, as there is now no polarization ending on the free surface, and the polarization is also fairly divergence-free in the interior. However, the usual 90° stress-free domain structures that are seen in bulk tetragonal ferroelectrics are not compatible in this geometry, i.e., the triangular closure domain does not have an angle of exactly 90° in the stress-free state and hence cannot form stress-free compatible interfaces with both the c^+ and c^- domains together. This leads to an angular defect or disclination and costs elastic energy. In the case of thin films, this elastic energy can be relaxed due to the traction free boundaries and leads to bending of the entire film (Figure 3.5). In the constrained case, the elastic energy cannot relax and there is larger electrostatic energy to compensate. In fact, this can be seen in the larger electrostatic potential outside the body in the constrained case.

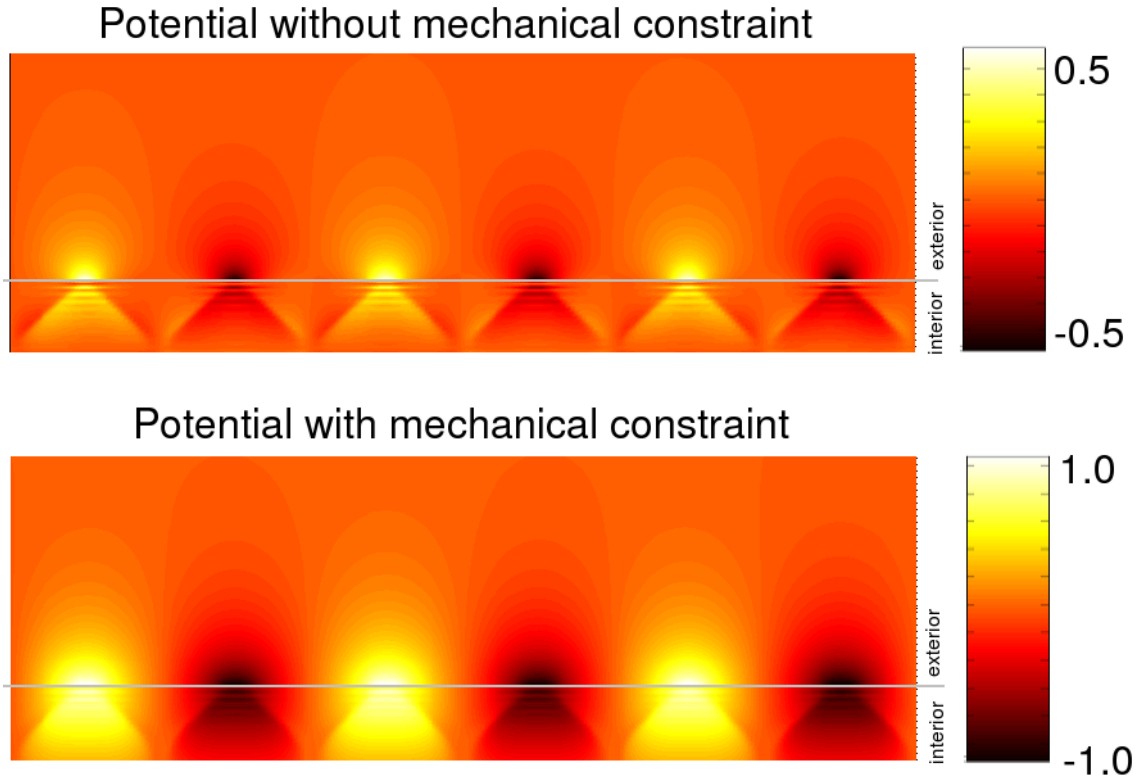

Figure 3.4: Electrostatic potential field caused by closure domains (*note the different magnitudes.*)

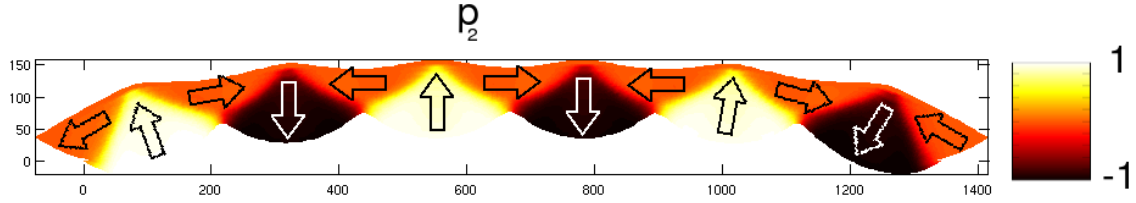

Figure 3.5: Bending of the film caused by incompatibility disclinations of the closure domains (vertical displacements magnified by a factor of 100).

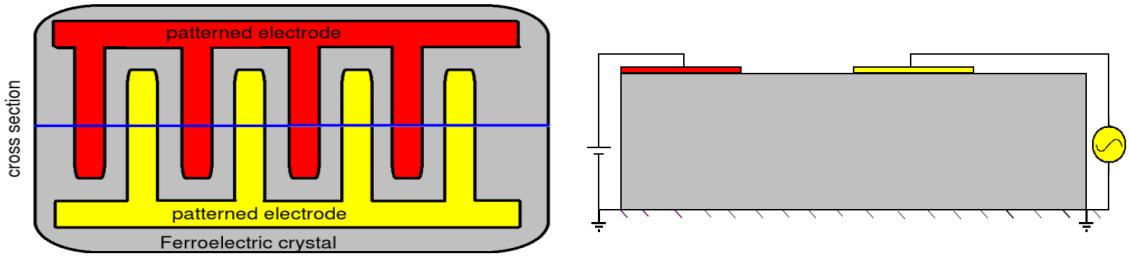

Figure 3.6: Schematic of an IDE device and the idealized two-dimensional calculation.

Understanding the electromechanics of closure domains is necessary to be able to understand the more complex mechanics that occurs at cracks, voids and other free surfaces. While this simple example demonstrates the capability of the boundary element technique, a systematic study is required, in particular with different volume fractions and different orientations of the free surface with respect to the crystal basis. Another important effect that is not considered here is the motion of charged defects due to the large electrostatic fields, which could change the final domain pattern.

3.5 Interdigitated electrode device

As a second example, we study the domain patterns that are formed in a device with interdigitated electrodes (IDE) when a constant DC bias is applied to one electrode and an AC voltage of the same magnitude is applied to the other electrode. Such a configuration of electrodes is of interest to produce periodically-poled lithium niobate (PPLN) ferroelectric crystals for use in optical second-harmonic generation (Nakamura et al., 2002), and has been proposed for tunable optical second-harmonic generation devices (Dayal and Bhattacharya, 2006b).

We consider a cross-section as marked on the schematic in Figure 3.6. We approximate the problem as being two-dimensional in this cross-section, and we use a rectangular computational domain that is periodic in the horizontal direction. We ground the entire bottom face and apply the DC bias to the left electrode and the AC forcing to the right electrode, with free surfaces between the electrodes. We leave all the faces traction-free.

Since nucleation of new domains plays an important role in this example, we use the method of *soft spots* as nuclei, following Zhang and Bhattacharya (2005). The soft spots are small regions that have the Landau expansion parameters changed in such a manner that the energy barrier for switching is much lower. In our system, we have positioned them just below the center of each electrode. For a discussion on why nucleation in phase-field models may be difficult and why soft spots and other techniques are required to induce switching, see Dayal and Bhattacharya (2006a).

We begin with a crystal that is entirely poled along the a-axis, with the polarization pointing towards the right. As we begin cycling, we find that the crystal forms complex domain patterns that evolve cyclically after an initial transient. Figure 3.7 shows snapshots from an entire cycle, represented by plots of both components of the polarization vector field at different times.

In the first snapshot at time t, Figure 3.7(a), the left electrode (running over the top surface for the first quarter) has constant positive DC bias and the right electrode (running over the top surface for the third quarter) is at the zero and climbing upwards on the AC cycle. The left (DC) electrode with a positive bias has a c^- domain structure beneath it, and the right (AC) electrode with zero voltage has a c^+ domain structure beneath it from the end of the previous cycle. There are also a-axis closure domains on the exposed regions of the surface with no electrode cover and some in the interior to satisfy compatibility approximately. As in the case of the closure domains, this domain pattern is not exactly compatible and we expect stresses or bending to occur.

In the second snapshot a quarter cycle beyond t, Figure 3.7(b), the right (AC) electrode is at the positive peak of the AC cycle and the domain has switched to c^-. Due to this switching, the right closure domain on the surface has also switched to maintain the polarization approximately divergence-free. The other domains change shape and size slightly to accommodate the new domain patterns.

In the third snapshot a half cycle beyond t, Figure 3.7(c), the right (AC) electrode is again at zero and falling. The domain patterns do not show much change, though the magnitude of the polarization in the c^- domain beneath the AC electrode has

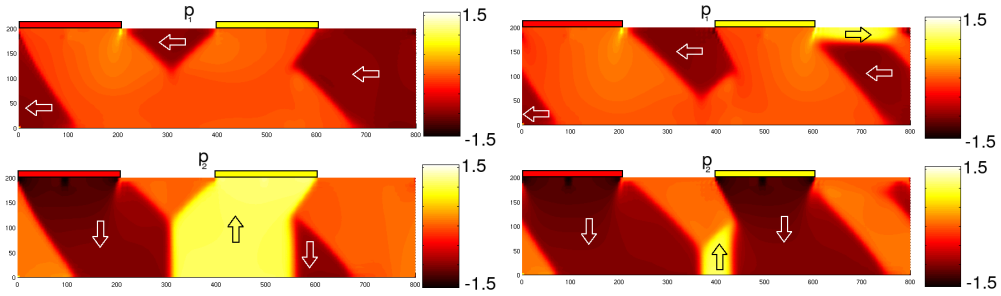

(a) Domain patterns at time t

(b) Domain patterns at quarter cycle beyond t

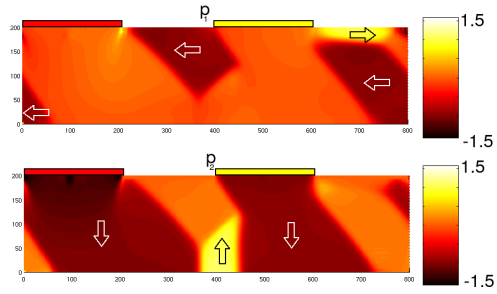

(c) Domain patterns at half cycle beyond t

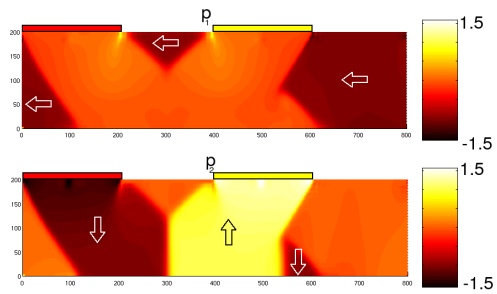

(d) Domain patterns at three quarter cycle beyond t

Figure 3.7: Snapshots of the polarization field. In each subfigure, the upper plot represents the horizontal component of $\mathbf{p}$ and the lower plot represents the vertical component of $\mathbf{p}$. The arrows are only to guide the reader. The entire movie is available from the authors.

reduced. Also, the c^+ has grown slightly.

In the fourth snapshot three quarters of a cycle beyond t, Figure 3.7(d), the right (AC) electrode is at the lowest point of the AC cycle. The c^- domain beneath the AC electrode has switched to c^+. The domain geometry looks very similar to that in the first snapshot at the beginning of the cycle. However, the magnitudes of the polarization are higher. This suggests to us that the domain geometry itself is somewhat independent of the magnitudes of the applied voltages and most of the domain motion occurs in short intervals after nucleation and switching. Hence, nucleation seems to control the kinetics of the process.

We see large polarizations building up at the edges of the electrodes due to the high electric fields in that region. More sophisticated models of ferroelectrics that incorporate fracture, breakdown and the motion of charged defects are required to understand the details of the crack formation process that often occurs at the edges of electrodes in ferroelectric and piezoelectric devices, and in those models the magnitude of the applied voltages will likely play a more important role.

3.6 Effect of a notch

Crack formation and growth due to combined electrical and mechanical loading is an important failure mechanism in ferroelectrics. The fracture process is more complex than in a purely mechanical setting due to the interaction between electrical and mechanical processes. The air gap caused by the opening of a crack can lead to the formation of closure domains, that in turn change the stress state in the body and in particular around the crack, leading to complex interactions. The large electric fields due to the free surfaces could also lead to the movement of charged defects that further complicate matters.

Crack growth in ferroelectrics under both cyclic and constant loading has been studied experimentally, with PZT/PLZT receiving much attention (see, for example, Lynch et al., 1995; Lupascu et al., 2003; Lynch, 1998; Oates et al., 2005). Experimental work in tetragonal ferroelectrics examining the 90° switching at the crack tip has

been studied by Fang et al. (2005, 1999) and Tan et al. (2000). Theoretical understanding of the crack growth phenomenon is difficult due to the need to incorporate local domain switching and formation of microstructure caused by the air gap. Efforts at understanding this process by making simplifying assumptions on the nature of the electrostatics, microstructure and surface structure are described in Wang and Landis (2004); Suo et al. (1992); Park and C.-T. Sun (1995); Hao et al. (1996); Zhu and Yang (1997, 1999); Rajapakse and Zeng (2001) and references there.

Resolving the role of domain switching at the crack tip is essential to be able to understand the crack growth process in ferroelectrics. This requires the ability to calculate the electric fields that arise at the free surfaces on the crack face, and is possible by using the boundary element technique. However, an accurate model of crack electromechanics would require a better representation of the geometry than is possible with the finite difference method. Further, electrostatics would have to be solved in the current configuration to model the air gap change due to opening of the crack.

We use an extremely simplified geometry as a first approximation to a crack to understand some of the issues that will arise in domain switching by exploiting the ability of the boundary element method. We use a rectangular computational domain with a thin rectangular notch removed. We ground the entire bottom face, and apply electrodes on either side of the notch. We use traction free boundary conditions over the entire boundary.

We point out that the notch is aligned with the direction of the crystallographic basis. As in the case of closure domains, we expect that the mechanics will be even more complex in the case of real cracks and notches that may not be aligned with this specific direction.

We do not use any nuclei in the calculations with the notch geometry, as the elastic fields were quite heterogeneous and did not seem to require any additional persuasion to nucleate domain structures.

We begin our computations with the polarization oriented along the horizontal direction to the right, with no applied loads or voltages. The large electric fields

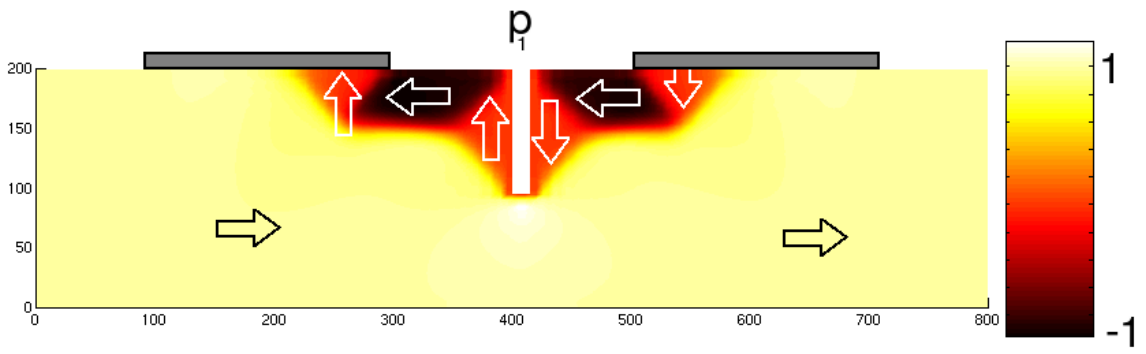

Figure 3.8: Equilibrium domain pattern that develops from an initially a-axis crystal. The gray blocks mark the electrodes that are grounded during equilibration.

caused by the polarization ending on the notch faces with this domain pattern lead to the formation of closure domains as we evolve the polarization. Figure 3.8 shows the equilibrated domain pattern that is obtained. As we discussed in Section 3.4, the domain pattern that we see is not compatible in a stress-free state. Thus, the mere presence of a notch causes stresses to develop even when no mechanical loads are applied. The polarization on the other hand closely approximates a divergence-free field and the crystal takes advantage of the presence of the electrodes in the formation of the closure microstructure on the surface.

Once the field has settled into an equilibrium state, we apply the same boundary conditions that were used to cycle the IDE device, i.e., a DC bias on the left electrode and AC forcing on the right electrode[3] as in Figure 3.9(a). After an initial transient, the domain patterns settle into a cyclic evolution pattern. Figure 3.10 shows some snapshots in the cycle, represented by plots of the individual components of the polarization vector field at different times.

The presence of the notch leads to interesting contrasts with the IDE geometry. The DC bias at the left electrode causes a c^- domain to form beneath it. As we can see from snapshots of the entire cycle, this domain hardly changes over the cycle. We also see that the presence of the notch has caused the entire upper half of the crystal to switch to a-axis oriented to the left. While this domain changes shape slightly in the vicinity of the AC electrode, it retains its structure over the rest of the crystal

[3]Though the electrodes seem to be positioned differently, the situations are equivalent due to the periodicity of the calculations in the horizontal direction.

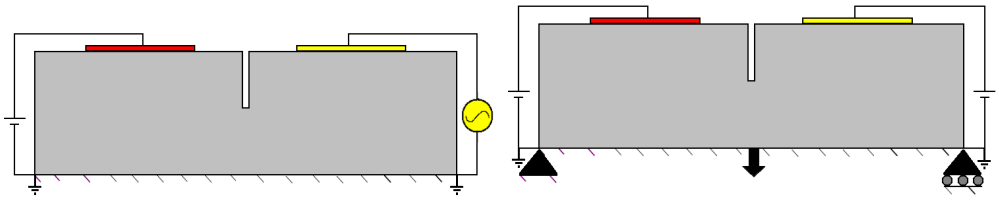

(a) Electrical boundary conditions during AC cycling

(b) Electromechanical boundary conditions during bending

Figure 3.9: Schematic of the different load cases on the notched specimen

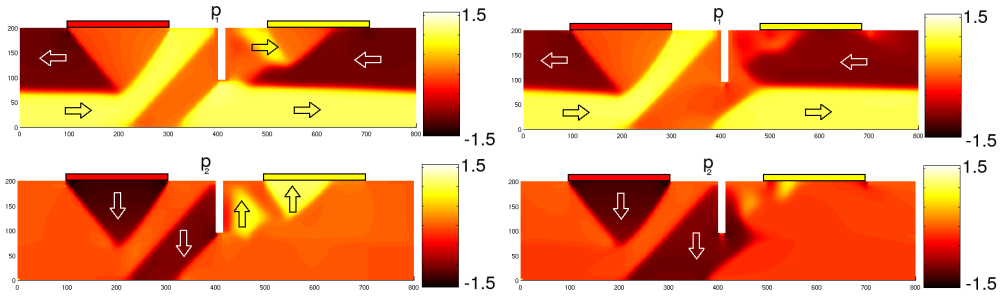

(a) Domain patterns at time t

(b) Domain patterns at quarter cycle beyond t

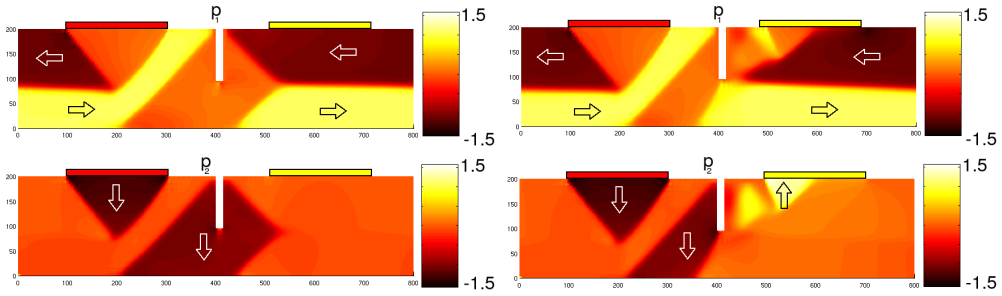

(c) Domain patterns at half cycle beyond t

(d) Domain patterns at three quarter cycle beyond t

Figure 3.10: Snapshots of the polarization field. In each subfigure, the upper plot represents the horizontal component of $\mathbf{p}$ and the lower plot represents the vertical component of $\mathbf{p}$. The arrows are only to guide the reader. The entire movie is available from the authors.

over the entire cycle.

In fact, the domain pattern in the entire crystal to the left of the notch does not change much at all under cycling and seems decoupled from the changes that occur due to the AC electrode. The domain pattern in the crystal to the right of the notch also does not change much except for some switching near the edge of the electrode close to the notch and the rearrangement of adjacent domains to maintain electrical compatibility.

The region between the notch and the right (AC) electrode is the only portion of the crystal that has large response to the AC forcing. In Figure 3.10(a), with zero AC voltage and climbing, the domain between the notch and the right electrode is c^+ from the previous cycle. As the voltage is increased, the domain switches to a-axis and the snapshot at the positive peak AC voltage, Figure 3.10(b), shows that the c^+ domain has almost completely switched to a-axis. In Figure 3.10(c), at zero AC voltage and dropping, the switching is complete and there is no c^+ remaining. Figure 3.10(d) at the lowest point of the AC cycle shows that the negative voltage has caused switching and the c^+ domain has reappeared.

As discussed in Shu and Bhattacharya (2001) for a simple flat-plate geometry, 180° switching is expected if purely electrical loads are applied and 90° switching is easier if mechanical and electrical loads are applied together. In the case of the IDE where purely electrical loads were applied, we see only 90° switching beneath the AC electrode. Here, in the presence of the notch, we see that the same magnitude of AC causes 90° switching and we do not observe 180° switching. We expect that the presence of the notch caused this change in behavior by raising stresses in the crystal due to closure domains formed on the notch faces. Also, the presence of the notch caused large regions of the crystal near the electrode to be dominated by a-axis domains that might also be a factor in this different behavior.

While this single case does not provide sufficient information for a general statement, we see that the notch caused the domain patterns to be much less responsive to AC forcing than in the case of the IDE geometry. In the design of ferroelectric devices, the possibility of degradation of performance due to geometric features and

defects needs consideration.

We now consider a calculation with a combination of mechanical and electrical loads that may provide insight into local domain switching of at crack tips. We begin with a notched crystal that is equilibrated from an a-axis poling as described above in Figure 3.8. We now apply a point mechanical load, i.e., at a single grid point, while keeping one corner of the crystal pinned (both displacements fixed) and another corner allowed only to translate horizontally, as shown in Figure 3.9(b). While applying this mechanical load, we ground both the electrodes at the surface and also keep the the entire bottom surface grounded as in the previous calculations. We apply sufficient load to cause domain switching at the tip. Once the specimen has been equilibrated, we superpose DC voltages applied at the electrodes on the surface and examine the domain switching at the notch tip.

Figure 3.11 shows the domain patterns that form when the mechanical load is applied without electrical loading. By comparing the domain patterns just below the tip of the notch in Figures 3.8 and 3.11, we see that local switching has occurred. The domain patterns elsewhere in the specimen have shifted slightly, but no major rearrangements have occurred at this magnitude of loading. For larger loads, we find changes in the domain pattern over much of the specimen. Smaller loads do not unambiguously cause switching.

It would seem that the mechanics in this simple case can be understood through ideas from beam theory. When we apply the load, it causes the specimen to bend. The region of the specimen above the middle, i.e., above the tip of the notch, cannot bear much load, and the load is mostly taken by the lower half. The lower portion of the specimen below the notch acts as a beam, and the region near the bottom has $\sigma_{11} > 0$ and the region just below the notch has $\sigma_{11} < 0$. This stress below the notch tip favors c-axis strains and causes some of the a-axis domain to switch.

This idea is confirmed by applying the a load of opposite sense at the same point to cause the notch to open. We find switching from a-axis to c-axis in the lowermost region of the specimen and the strain just below the notch tip goes further away from c-axis.

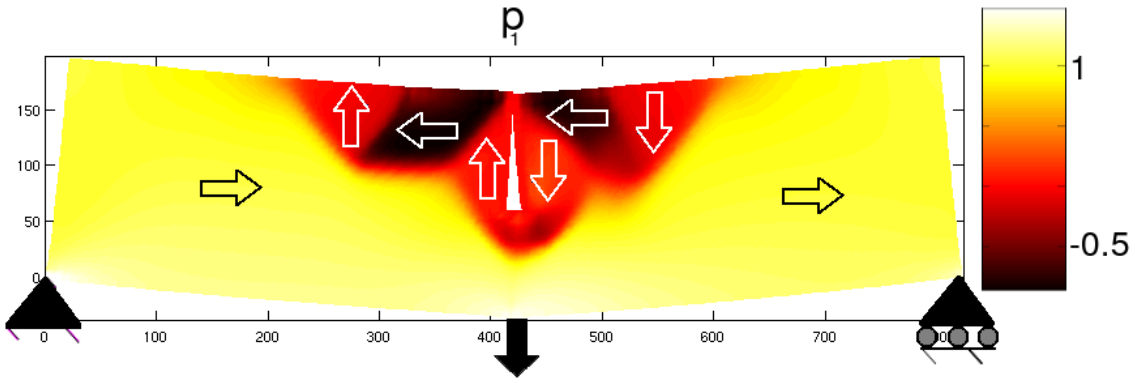

Figure 3.11: Domain pattern that develops when a point mechanical load is applied while keeping the electrodes grounded. Note that the displacements are *not* magnified.

By examining the distorted specimen in Figure 3.11, we see that the crystal has undergone large bending. As ferroelectric materials are quite brittle, we do not expect such large distortions to occur and it is likely that the specimen will mechanically fail before we see domain switching at the notch tip.

We now superpose different DC bias voltages to both of the electrodes in an attempt to reverse the switching. It is unlikely that it is possible to reverse the domain patterns to the mechanically unloaded state in the entire specimen by applying the voltages at the specific positions that we have chosen for the electrodes in this example. Instead, we examine the switching at the notch tip only.

For moderate voltage (compared to the applied voltage in the cycling) applied at the electrodes, we are able to reverse the mechanically induced switching at the notch tip. Figure 3.12 shows the complex domain patterns that develop elsewhere in the specimen as a result of applied voltages superposed over the large mechanical load. The distortion of the specimen induced by the mechanical loading does not show any significant reversal due to the application of voltage.

Domain switching at a notch tip geometry requires small electric fields that do not generate much stress. Stress-induced switching requires unrealistically high stresses. Hence domain switching at a notch tip is likely to be dominated by the local geometry (that influence surface charges) and will be less affected by far field stresses.

While local switching at a crack tip in a ferroelectric material is a complex process,

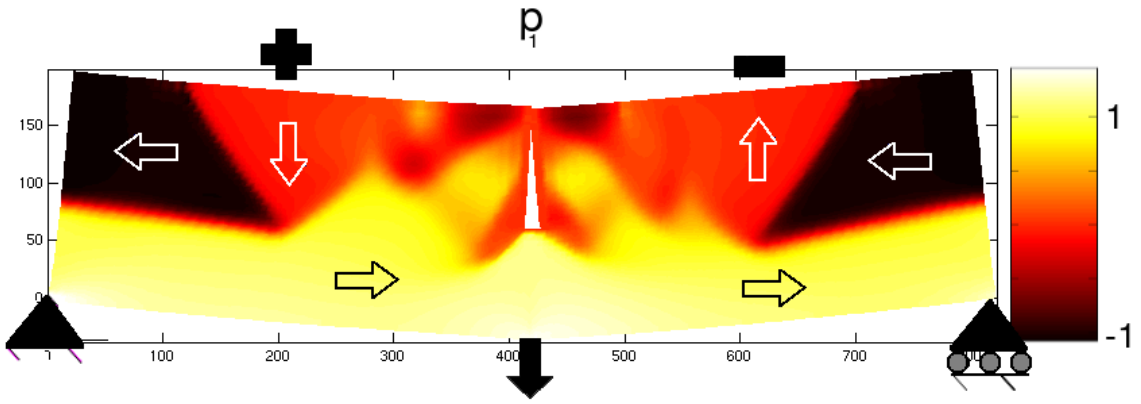

Figure 3.12: Domain pattern after back-switching the domain at the notch tip using DC bias at both electrodes. Note that the displacements are *not* magnified.

this calculation regarding the balance of different electrical and mechanical loads shows that it may not be sufficient to consider the mechanics as dominating the fracture process, but other factors that influence the electrostatics also play a role.

In a real crack, the domain switching leads to local stresses due to closure domain disclinations and the associated rearrangements. This microstructure is influenced by the electrostatics and the crystallographic surface structure, that in turn depend strongly on local crack geometry and orientation with respect to the crystal basis.

3.7 Discussion

We have formulated a boundary element technique to understand the effect of free surfaces in ferroelectric crystals. We find that the ability to solve electrostatics using this technique raises many interesting questions regarding the interplay between mechanics and electrostatics at defects.

We have solved some simple examples to illustrate this method and also provide insight into the electromechanics in ferroelectrics. We find that closure domains form even in the simple geometry where the volume fractions of c^+ and c^- are equal, and the free surface is aligned with the crystallographic basis. More complex domain patterns and orientations will likely lead to more complexity. As closure domains form the basis for understanding the electromechanical behavior of free surfaces in various

settings including cracks, electrode edges, and micromachined features, a fundamental understanding is necessary.

A second example that we calculated illustrated the complex domain patterns that form even in simple geometries with straightforward boundary conditions. We see that design of IDE devices with optimal behavior may not be straightforward.

We also examined the effect of a notched geometric defect. We see that the behavior of the domain patterns is quite rich even with the various simplifications required. More sophisticated techniques such as the finite element that can provide more realistic models of cracks seem justified in light of the complex behavior that can not be predicted using ideas from conventional fracture mechanics.

A major simplification that we have made are neglecting the role of charged defects. These defects play a significant role in the electromechanics of ferroelectric materials, and their role is further enhanced in the presence of large electric fields as were seen in the geometries considered. Exploratory calculations of modeling the piezo-force microscope (PFM) response of ferroelectrics and comparison with experiments indicate that charged defects play an important role in understanding closure domains. It seems to be possible to incorporate ideas from Xiao et al. (2005) concerning charged defects in ferroelectrics within the boundary element framework. However, this will make the problem nonlinear and poses interesting challenges.

A second major simplification that we have made is assuming that the current and reference configurations can be described within the framework of linear elasticity. This led to simplifying the formulation of the electrostatics problem. In situations of interest, for example crack opening and growth, this approximation may need to be removed. This would require solution of the electrostatics problem in the current configuration. This may require remeshing at each time step. Work by Li and Aluru (2002) and others in the context of MEMS shows that it may be more efficient to formulate the problem in the reference.

Bibliography

Bhattacharya, K., James, R. D., 2005. The material is the machine. Science 307 (5706), 53–54.

Dayal, K., Bhattacharya, K., 2006a. Kinetics of phase transformations in peridynamic formulation of continuum mechanics. J. Mech. Phys. Solids (in press).

Dayal, K., Bhattacharya, K., 2006b. Tunable quasi-phase-matching through ferroelectric domain switching, in preparation.

DeSimone, A., Kohn, R. V., Muller, S., Otto, F., 2005. Recent analytical developments in micromagnetics. In: Bertotti, G., Magyergyoz, I. (Eds.), Science of Hysteresis. Elsevier.

Fang, F., Yang, W., Zhang, F. C., Luo, H. S., 2005. Fatigue crack growth for $BaTiO_3$ ferroelectric single crystals under cyclic electric loading. J. Am. Ceram. Soc. 88 (9), 2491–2497.

Fang, F., Yang, W., Zhu, T., 1999. Crack tip 90° domain switching in tetragonal lanthanum-modified lead zirconate titanate under an electric field. J. Mater. Res. 14 (7), 2940–2944.

Fidler, J., Schrefl, T., 2000. Micromagnetic modelling - the current state of the art. J. Phys. D Appl. Phys. 33 (15), R135–R156.

Hao, T. H., Gong, X., Suo, Z., 1996. Fracture mechanics for the design of ceramic multilayer actuators. J. Mech. Phys. Solids 44 (1), 23–48.

Hu, H. L., Chen, L. Q., 1998. Three-dimensional computer simulation of ferroelectric domain formation. J. Am. Ceram. Soc. 81 (3), 492–500.

Hubert, A., Schafer, R., 1998. Magnetic Domains. Springer.

Kalinin, S., Bonnell, D., Alvarez, T., Lei, X., Hu, Z., Ferris, J., Zhang, Q., Dunn, S., 2002. Atomic polarization, charge compensation, and local reactivity on ferroelectric surfaces: a new route toward complex nanostructures. Nano Lett. 2, 589–594.

Kane, J. H., 1994. Boundary element analysis in engineering continuum mechanics. Prentice-Hall.

Li, G., Aluru, N. R., 2002. A lagrangian approach for electrostatic analysis of deformable conductors. J. Microelectromech. S. 11 (3), 245–254.

Li, Y. L., Hu, S. Y., Liu, Z. K., Chen, L. Q., 2002. Effect of substrate constraint on the stability and evolution of ferroelectric domain structures in thin films. Acta Mater. 50 (2), 395–411.

Lupascu, D., Aulbach, E., Rodel, J., 2003. Mixed electromechanical fatigue in lead zirconate titanate. J. Appl. Phys. 93 (9), 5551–5556.

Lynch, C. S., 1998. Fracture of ferroelectric and relaxor electro-ceramics: influence of electric field. Acta Mater. 46 (2), 599–608.

Lynch, C. S., Chen, L., Suo, Z., McMeeking, R. M., Yang, W., 1995. Crack growth in ferroelectric ceramics driven by cyclic polarization switching. J. Intel. Mat. Syst. Str. 6 (2), 191–198.

Nakamura, K., Kurz, J., Parameswaran, K., Fejer, M. M., 2002. Periodic poling of magnesium-oxide-doped lithium niobate. J. Appl. Phys. 91 (7), 4528–4534.

Oates, W. S., Lynch, C. S., Kounga Njiwa, A. B., Lupascu, D. C., 2005. Anisotropic fracture behavior in ferroelectric relaxor PZN-4.5%PT single crystals. J. Am. Ceram. Soc. 88 (7), 1838–1844.

Park, S., C.-T. Sun, 1995. Fracture criteria for piezoelectric ceramics. J. Am. Ceram. Soc. 78 (6), 1475–1480.

Rajapakse, R. K. N. D., Zeng, X., 2001. Toughening of conducting cracks due to domain switching. Acta Mater. 49 (5), 877–885.

Shu, Y. C., Bhattacharya, K., 2001. Domain patterns and macroscopic behavior of ferroelectric materials. Philos. Mag. B 81 (12), 2021–2054.

Suo, Z., C.-M. Kuo, Barnett, D. M., Willis, J. R., 1992. Fracture mechanics for piezoelectric ceramics. J. Mech. Phys. Solids 40 (4), 739–765.

Tan, X., Xu, Z., Shang, J., Han, P., 2000. Direct observations of electric field-induced domain boundary cracking in $\langle 001 \rangle$ oriented piezoelectric $Pb(Mg_{1/3}Nb_{2/3})O_3$-$PbTiO_3$ single crystal. Appl. Phys. Lett. 77 (10), 1529–1531.

Wang, J., Landis, C., 2004. Fracture of ferroelectric and relaxor electro-ceramics: influence of electric field. Acta Mater. 52, 3435–3446.

Wang, J., S.-Q. Shi, L.-Q. Chen, Li, Y., T.-Y. Zhang, 2004. Phase-field simulations of ferroelectric/ferroelastic polarization switching. Acta Mater. 52 (3), 749–764.

Wrobel, L. C., 2002. The Boundary Element Method: Applications in Thermo-Fluids and Acoustics. Vol. 1. John Wiley & Sons.

Xiao, Y., Shenoy, V. B., Bhattacharya, K., 2005. Depletion layers and domain walls in semiconducting ferroelectric thin films. Phys. Rev. Lett. 95, 247603.

Zhang, W., Bhattacharya, K., 2005. A computational model for ferroelectric domains. Part I: model formulation and domain switching. Acta Mater. 53, 185–198.

Zhu, T., Yang, W., 1997. Toughness variation of ferroelectrics by polarization switch under non-uniform electric field. Acta Mater. 45 (11), 4695–4702.

Zhu, T., Yang, W., 1999. Fatigue crack growth in ferroelectrics driven by cyclic electric loading. J. Mech. Phys. Solids 47 (1), 81–97.

Chapter 4

Conclusions

The ability to manipulate the microstructure of active materials can open the way to the design of new devices at smaller lengthscales (Bhattacharya and James, 2005). This will require the development of models that capture the essential physics at the lengthscales of relevance. In this thesis, we have examined two problems that arise in this general area.

We have examined the evolution of microstructure in a dynamic setting using the peridynamic theory of continuum mechanics. We have confined ourselves to one dimension for simplicity, to obtain insights into the nature of phase transformations and microstructure evolution in this theory. We find that the evolution of microstructure can be understood in the framework of a kinetic relation and a nucleation criterion.

In particular, the propagation of phase boundaries in dynamic calculations can be directly calculated using a traveling wave ansatz, and the kinetics that result from both approaches match. However, both techniques rely on a discretization of a continuum equation, and are both subject to the numerical artifacts that can arise in such a setting.

A more conclusive result on the ability of peridynamics to support kinetic relations through a traveling wave framework will require existence proofs of such waves, and this is a major problem that is outside the scope of this thesis.

Another open question relates to how much information regarding the movement of phase boundaries is contained in a kinetic relation calculated in a traveling wave framework. The traveling wave framework has built into it the assumption that the

phase boundary is propagating at a steady velocity and that the strain fields on either side tend to a constant value (with some oscillations about the mean). It is not clear how to apply the classical continuum idea of a driving force to a transient setting in a nonlocal theory such as peridynamics. The classical definition of a driving force depends on the fact that interfaces in that theory are sharp. In theories such as peridynamics or a regularized model where the structure of the interface is modeled, the traveling wave ansatz has the assumption that strain fields tend to a constant value far away, and that allows us to generalize the idea of the driving force slightly. However, in a truly transient setting, the strain fields may not have this nice structure and that leads to fundamental difficulties. In particular, the relation between the stress as the derivative of the strain energy density with strain that is available in classical continuum mechanics no longer holds in peridynamics when the strain field has variations over relatively short lengthscales (see Silling, 2000).

This question may be related to the fact that the kinetic relation (representing finite dissipation at macroscopic scales) comes from the averaging away of the microscopic oscillations about the mean strain field. In transient settings where the strain field does not tend to a mean, it is difficult to make the distinction between macroscopic averages and microscopic oscillations.

Experimental observations of phase boundary movement suggest that there is a critical nonzero driving force required to initiate motion in a stationary phase boundary. We recall that the kinetic relation calculated in peridynamics did not show this "stickiness", even with the viscous damping mechanism. To the best of our knowledge, available microscopic theories that consider phase boundary motion in an isolated system, i.e, with no other defects, are inadequate to understand this. A possible microscopic understanding of this effect involves the interaction of phase boundaries with pinning defects (for example see Bhattacharya, 1999).

The nucleation of phase boundaries is understood in terms of the linear stability of displacement fields. We find that analytical scaling results that we have derived from linear stability arguments match well the numerical predictions from dynamics. We find that nucleation can be described in terms of a defect size, and in peridynamics

this defect size depends on the ambient displacement field in the neighborhood of the defect in contrast to PDE models of continuum mechanics. This provides a different perspective on nucleation in terms of linear stability, in contrast to conventional methods.

In future work, it may be useful to apply this idea to a multi-dimensional setting in an attempt to derive nucleation criteria for more realistic systems. Multi-dimensional settings would require accounting for anisotropy among the many other complications that arise in higher dimensions, and the characterization of nucleation in terms of a single scalar defect size may not be possible.

There is little description regarding the connection between the work on kinetics and nucleation and experiments in this area. The reasons for this lack include the non-availability of experimental data to compare with due to the many experimental challenges that arise in a study in this area. Further, the peridynamic theory itself is not yet well understood and characterized theoretically. Further activity in both these directions is required before the possibility of making fruitful comparisons arises. However, both directions are areas of active research and the outlook is optimistic.

It may also be possible to apply the idea of linear stability to understand the kinetics of steadily propagating phase boundaries as traveling waves. As in nucleation, phase boundaries contain a region in the spring-space that is unstable. The size of the unstable region depends on the end states of the phase boundary. However, as in nucleation again, the phase boundary structure as a whole is still stable in the traveling wave frame, despite the unstable springs. By testing the linear stability of a phase boundary against the appropriate perturbations, it may be possible to obtain the allowed range of end states of the phase boundary. This would provide allowed regions (and possibly bounds) for the kinetic relation.

Our primary motivation to study the peridynamic system was the possibility of making connections to atomistics. While it is not clear if there is indeed a strong connection, both peridynamics and atomistics share some important features, in particular nonlocal interactions. It may be possible to apply some of the techniques developed here in the context of peridynamics to atomistic systems. One particu-

lar difficulty that would arise is the accounting of temperature in atomistic systems. The Nose-Hoover method (described in Frenkel and Smit, 1996, and elsewhere) of modeling thermal interactions between the atomistic system of interest and the surroundings poses interesting challenges.

A second problem that we have examined in the this thesis concerns the domain patterns that form in ferroelectrics at geometric defects. Previous work in studying microstructure has focused on periodic systems to enable efficient computation. As the need for understanding microstructure in more complex geometries arises, it is necessary to extend this work. We have applied a boundary element electrostatic solver that allows the modeling of free surface microstructure in ferroelectrics.

We have presented examples of calculations that are possible using this technique. In particular, an example of closure domain formation at a free surface, the electrical cycling of a patterned electrode device and the effect of a notch have been presented. We see that geometric defects can lead to complex microstructure and evolution.

While these examples show the interesting electromechanical response that occurs at free surfaces, and the computational ability that comes of applying the boundary element method, there is much progress that needs to made in terms of incorporating physics and implementing solution techniques.

An important physical effect that we have not considered in this thesis is the movement of charged defects. Many ferroelectrics are wide bandgap semiconductors and contain oxygen vacancies. Large electric fields cause these effects to gain importance. Geometric defects such as electrode edges and notch tips usually imply large electric fields. Understanding real devices and their electrical and mechanical reliability will require combining this physics, possibly through continuum models of the kind formulated by Xiao (2004).

A second physical effect that needs to be accounted for is the interaction of light with ferroelectrics or photorefractivity. Light passing through a ferroelectric can cause charged defects to diffuse and modify the optical properties as well as the microstructure. Applying ferroelectrics to optical devices that have been proposed (for example Dayal and Bhattacharya, 2006) require the ability to model photorefractivity.

The use of the finite difference method to solve the elasticity equations imposed restrictions on the geometries that could be studied. Models of cracks that incorporate realistic fracture mechanics will require the ability to model arbitrary geometries as is possible with the finite element method. Coupling the phase field and boundary element implementations to a finite element solution of elasticity can open the way to a comprehensive understanding of the electromechanics of cracks in different geometries and orientations.

Bibliography

Bhattacharya, K., 1999. Phase boundary propagation in heterogeneous bodies. Proc. Royal Soc. Lond. A 455, 757–766.

Bhattacharya, K., James, R. D., 2005. The material is the machine. Science 307 (5706), 53–54.

Dayal, K., Bhattacharya, K., 2006. Tunable quasi-phase-matching through ferroelectric domain switching, in preparation.

Frenkel, D., Smit, B., 1996. Understanding molecular simulation. Academic Press.

Silling, S. A., 2000. Reformulation of elasticity theory for discontinuities and long-range forces. J. Mech. Phys. Solids 48, 175–209.

Xiao, Y., 2004. The influence of oxygen vacancies on domain patterns in ferroelectrics. Ph.D. thesis, California Institute of Technology.